Department of Physics and Astronomy
Heidelberg University

Bachelor Thesis in Physics
submitted by

Celina Welschoff

born in Gütersloh (Germany)

2023

Measurement of the Background Muon Flux for the proposed SHADOWS Experiment

This Bachelor Thesis has been carried out by Celina Welschoff at the
Physikalisches Institut in Heidelberg
under the supervision of
Prof. Ulrich Uwer

Abstract

In the context of searching for possible dark matter particles a new beam-dump experiment, using a 400 GeV proton beam, is proposed at CERN. The SHADOWS experiment is going to search for Feebly Interacting Particles, which are, depending on the model, either candidates for Dark Matter or mediator particles between the matter and the dark matter sector and are possibly produced at the beam-dump. Their production and decay into Standard Model particles might be strongly suppressed and any background leading to comparable decay signatures is disturbing. To reduce misidentification with background particles, it is essential to study the background precisely and reduce it to a minimum. This thesis presents a measurement of the background muon flux at the future position of the SHADOWS detector. It includes a detailed explanation of the construction and testing of the used measurement setup which is composed of plastic scintillators read out by silicon photomultipliers. The measurement carried out in the context of this thesis reveals that the measured background muon flux agrees with the simulation and is an important result for further studies.

Zusammenfassung

Auf der Suche nach hypothetischen dunkle Materie Teilchen wird ein neues Beam-Dump Experiment am CERN vorgeschlagen. Das SHADOWS Experiment wird nach sogenannten Feebly Interacting Particles (sehr schwach interagierenden Teilchen) suchen, die möglicherweise bei der Kollision des 400 GeV Proton-Strahls mit dem Beam-Dump entstehen. Feebly Interacting Particles agieren je nach Modell entweder als Mediatoren zwischen Dunkler Materie und Materie oder sind mögliche Dunkle Materie Teilchen. Ihre Entstehung und ihr Zerfall sind möglicherweise stark unterdrückt, deshalb ist jeder Hintergrund, der zu ähnlichen Zerfallssignaturen führt, störend. Um eine Missidentifikation mit Hintergrund Teilchen zu vermeiden, ist es essenziell den Hintergrundfluss zu untersuchen und auf ein Minimum zu reduzieren. Diese Arbeit beinhaltet eine Messung des Hintergrund Myonen Flusses an der zukünfigen Position des SHADOWS Detektors, sowie eine detaillierte Charakterisierung des verwendeten Messaufbaus aus Plastikszintillatoren und Siliziumphotomultipliern. Die im Rahmen dieser Arbeit durchgeführte Messung des Hintergrund Myonen Flusses stimmt mit den Simulationen überein und ist damit ein wichtiges Ergebnis für weitere Untersuchungen.

Contents

1. Introduction

The Standard Model of Particle Physics describes the composition of matter and the interaction of the fundamental building blocks. It is one of the most successful theories in physics [1]. It has been successfully tested since its formulation in the 1970s. The Standard Model describes most current experimental data. However, there are some phenomena such as the existence of Dark Matter which escape the description of the theory. Therefore, physicists all over the world are trying to find additions to it as well as solutions to unsolved problems.

One possible solution to overcome the problem lies in searching for new particles, currently not included in the Standard Model, but which could extend it. This includes particles belonging to dark matter as well as mediators between matter and dark matter. Examples for such particles are Feebly Interacting Particles (FIPs), which interact feebly with the currently known matter particles [2]. This is where the SHADOWS experiment comes in handy. SHADOWS [3] is a proposed beam-dump experiment at CERN and is designed for the search of FIPs via their decay products. It is planned to be placed in the TCC8 tunnel upstream of the ECN3 experimental hall and will be served by a 400 GeV proton beam from the Super Proton Synchrotron (SPS) colliding on a beam-dump to generate possible Feebly Interacting Particles [3].

This thesis aims to determine the background muon flux produced in the proton beam-dump at the future SHADOWS position. As muons are the biggest contribution to the background, studying and reducing the background muon flux in the SHADOWS acceptance is crucial to minimise misidentification of background particles with decay products of a FIP. In the context of this thesis a measurement of the background muon flux at the future SHADOWS position is carried out. To fulfil this goal a measurement setup consisting of scintillators read out by silicon photomultipliers is designed, constructed and tested. The construction and testing are performed in the framework of this thesis.

The thesis is structured as following: In section 2 the general physics context for this thesis is described. The principles of particle detection used in this thesis are described in section 3, which is then followed by section 4 in which the SHADOWS experiment is introduced. Furthermore, the experimental area and its relevant technical parts for this thesis are introduced in this chapter. The thesis continues with a detailed explanation of the used measurement setup including its construction and testing in section 5. It ends with section 6 which deals with the main goal of this thesis, the measurement and determination of the background muon flux at the future SHADOWS detector position.

2. Theoretical Background

2.1. The Standard Model

The Standard Model is currently the most accurate model to describe the composition of matter and its interaction. It consists of 12 fermions and their corresponding antiparticles, four gauge bosons and the Higgs-Boson. It describes three fundamental forces: The electromagnetic force, the weak force and the strong force. Gravitation, which is the last fundamental force, is not described by the Standard Model [1].

Fermions are half-integer-spin particles. All fermions from the standard model have a spin of 1/2. There are 12 fermions, which are divided into six leptons and six quarks. They are split up into three generations with different masses but similar physical characteristics. The leptons are divided into charged leptons (e^-, μ^-, τ^-) with a charge of -1 and their corresponding neutral and massless neutrinos (ν_e, ν_μ, ν_τ). The quarks consist of up-type quarks (u, c, t) with an electromagnetic charge of +2/3 and down-type quarks (d, s, b) with an electromagnetic charge of -1/3.

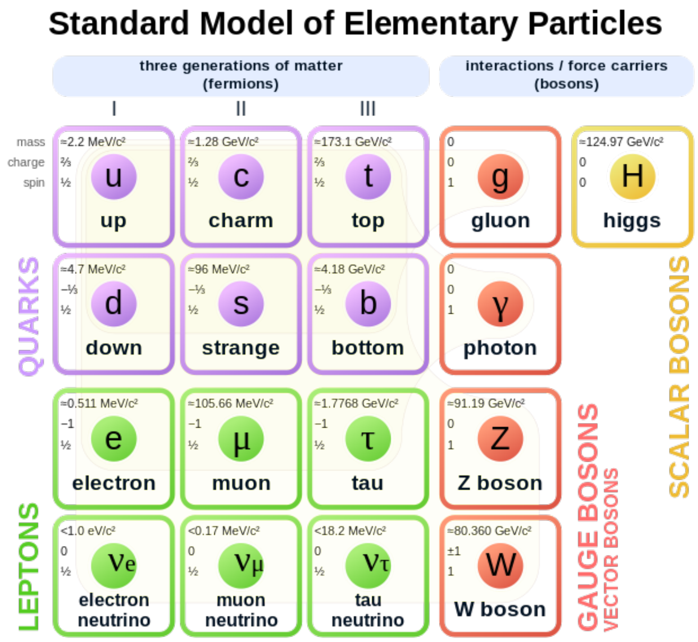

Figure 2.1: Standard Model of Elementary Particles [4]

The gauge bosons are spin-1 particles, and mediate the fundamental forces of the Standard Model. The photon γ is massless, has no electromagnetic charge and mediates the electromagnetic interaction. It only acts on particles which have an electromagnetic charge. The weak interaction is mediated by the massive neutral Z-boson and the massive and electromagnetic charged $W^{\pm}$-boson which is responsible for a flavour change between particles. The strong interaction is mediated by the eight gluons. It only acts on particles which have a colour charge which are quarks and gluons. The strong interaction is responsible for the formation of hadrons. Neutrinos do only interact via the weak interaction. The mass of particles is described by the coupling of particles to the Higgs-field.

Leptons can be found as free particles whereas quarks form bound, colour neutral states, so called hadrons. Baryons are hadrons consisting of three quarks and mesons are hadrons made of a quark anti-quark pair. The most famous examples for baryons are the proton and the neutron, which consist of *uud* and *duu* quarks, respectively. Together with the electrons they make up atoms, which form what we know as matter.

2.2. The Muon

The muon is one of the fundamental particles included in the standard model. Together with the muon neutrino it forms the second generation of leptons. The muon has around 207 times the mass of an electron and can therefore decay into an electron via the emission of two neutrinos. Muons are produced naturally from cosmic rays and reach the earth with a flux of $100 \ \frac{\text{muons}}{\text{s}\cdot\text{m}^2} = 0.01 \ \frac{\text{muons}}{\text{s}\cdot\text{cm}^2}$ [5]. Cosmic muons at sea level are the result of secondary cosmic rays. Primary cosmic rays mainly contain protons which then produce pions and kaons due to interaction with molecules from the atmosphere [6],

$$p + p \rightarrow p + n + \pi^+ \tag{2.1}$$

$$p + n \rightarrow p + p + \pi^- \tag{2.2}$$

$$p + p \rightarrow p + \Lambda + K^+ \tag{2.3}$$

which then decay mainly into muons.

$$\pi^+ \rightarrow \mu^+ + \nu_\mu \tag{2.4}$$

$$\pi^- \rightarrow \mu^- + \bar{\nu_\mu} \tag{2.5}$$

$$K^+ \rightarrow \mu^+ + \nu_\mu \tag{2.6}$$

It can be seen from the presence of neutrinos, that these decays happen via the weak interaction mediated by a $W^{\pm}$-boson.

Cosmic muons are only able to reach the earth surface due to their highly relativistic characteristics, otherwise they would have already decayed before reaching the earth. They can decay via the following decay branches:

$$\mu^- \rightarrow e^- + \nu_\mu + \bar{\nu_e} \tag{2.7}$$

$$\mu^+ \rightarrow e^+ + \nu_e + \bar{\nu_\mu} \tag{2.8}$$

Beyond that muons can be produced artificially by particle collisions. Muons do only interact via the weak and electromagnetic force. They lose their kinetic energy mainly via ionisation, because the energy loss by bremsstrahlung is very small due to their high mass. The energy loss of muons due to ionisation is according to the Bethe-Bloch formula around 2 $\frac{\mathrm{MeV \cdot cm^2}}{\mathrm{g}}$ (for a minimal ionising muon) [5]. Therefore, high energetic muons can pass through a large amount of material before they lose all their energy. Due to that, muons are difficult to shield.

2.3. The Physics of Feebly Interacting Particles

As the Standard Model has some incompletenesses, for example it does not describe dark matter, there is need for an additional theory [7]. Looking more detailed into the dark matter problem studies have shown that only around 5 % of the energy of the universe can be explained with Standard Model particles. The rest could be made out of dark matter and dark energy. But the Standard Model does not provide any particle candidates for dark matter.

One possible option is the search for heavy Dark Matter candidates which is for example done at the LHC experiments. The second option realised with the SHADOWS experiment is to search for Feebly Interacting Particles (FIPs). These FIPs are supposed to be either light Dark Matter candidates or the mediators between Standard Model (SM) particles and Dark Matter. Those FIPs can be either massless or massive, do not carry electromagnetic or strong interaction charges, have a very long lifetime and do only interact with SM via couplings (not via electroweak or strong interaction), which are small compared to the electroweak coupling.

FIPs are described via the Portal Formalism which proposes four portals. The Portal Formalism describes the total interaction between Standard Model (SM) and the Dark Sector (DS) via these portals. The particles emerging from the portal formalism are then supposed to be the mediators between the SM and DS and are also candidates for Dark Matter [3].

The four portals are summarised in Table 2.1:

Portal	Particle
Vector	Dark Photon A'
Scalar	Dark Higgs S
Pseudo Scalar	Axion a
Fermion	Heavy Neutral Lepton (HNL)

Table 2.1: Portals in the Portal Formalism and possible resulting Particles [2]

The portals describe four different possible particles which are distinguished by different quantum numbers, but with common characteristics.

Those hypothetical particles can decay into SM particles. The resulting particles can be detected and conclusions about the original particle can be made. As the FIPs do not carry electroweak and strong charge they can only decay in pairs of negative and positive charged particles or neutral particles. The main decay modes are summarised in Table 2.2.

Portal	Main decay mode
Vector	l^+l^-, $\pi^+\pi^-$, K^+, K^-
Scalar	l^+l^-, $\pi^+\pi^-$, K^+, K^-
Pseudo Scalar	l^+l^-, $\gamma\gamma$, $\pi^+\pi^-$, K^+, K^-
Fermion	$l^\pm\pi^\mp$, $l^\pm K^\mp$, $l^\pm\rho^\mp$, $l^+l^-\nu$

Table 2.2: Portals in the Portal Formalism and possible decay modes of resulting particles [3]. l meaning a lepton

One example for a FIP is the Axion Like Particle a (ALP) from the pseudo scalar portal. It can be produced in the decay of mesons, especially from Kaons and B-Mesons [8]. The decay modes are seen in Equation 2.9 and Equation 2.10. The process is illustrated in Figure 2.2.

$$K \rightarrow \pi a \tag{2.9}$$

$$B \rightarrow K^* a \tag{2.10}$$

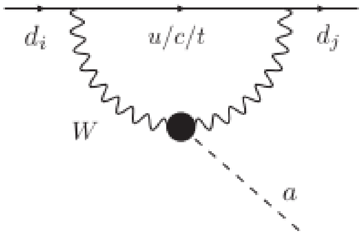

Figure 2.2: Axion like particle production in down type quark decay as it happens in Equation 2.9 and Equation 2.10 [9]

The produced ALP decays into Standard Model particles as explained in Table 2.2. It can be seen from Table 2.2 that the majority of the FIP decays contain only two particles in the final state. This is the signature, the SHADOWS Experiment (introduced in section 4) is going to look for, especially the dimuon final state [3].

3. Particle Detection

As this thesis aims to measure the background muon flux at the position of the future SHADOWS experiment a measurement setup is designed and constructed to detect muons. It consists of a system of a plastic scintillator, a wavelength-shifting fibre and a silicon photomultiplier. Therefore, the working principles of the different parts are described in detail in this chapter. Furthermore, the used measurement principle is described.

3.1. Scintillator

Scintillators are commonly used to detect charged particles or photons. There are two types of scintillators: inorganic and organic scintillators. In this thesis an organic scintillator is used i.e. a plastic scintillator. If a charged particle travels through the plastic scintillator, it can trigger the emission of scintillation light. The particle which traverses the scintillator looses energy via ionisation or excitation of the molecules of the scintillator. In the latter case it excites an electron of the molecules of the scintillator from the ground state to a higher instable energy level. The particle traversing the scintillator does therefore lose energy. The transition of the scintillator molecule to the ground state happens in two steps. Within a few picoseconds the electron falls back to a lower energy level without radiation. What can be seen as scintillating light is the transition back to the ground state, which takes place within a few nanoseconds. The process is illustrated in Figure 3.1. For example it can be seen that the electron from the ground state S_{00} is excited to S_{12}, falls back to S_{10} without radiation and falls back to S_{00} while emitting the scintillating light [5].

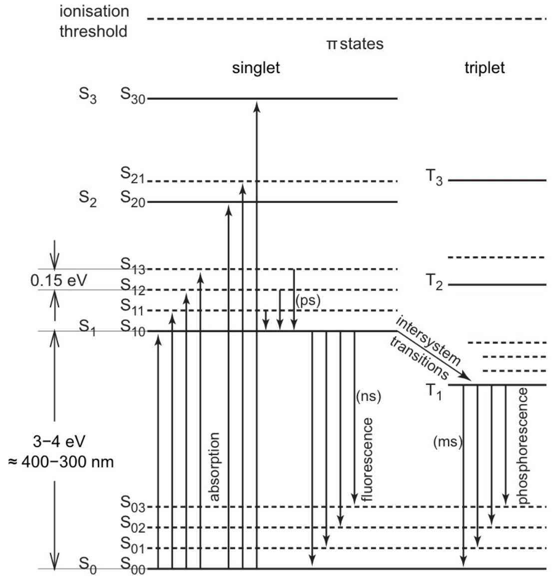

Figure 3.1: Energy Levels of π-electrons in an organic scintillator [5].

The emitted photon has a lower energy than the original excitation energy necessary to excite the scintillator molecule. This leads to the so called Stokes-Shift [5] between absorption and emission seen in Figure 3.2.

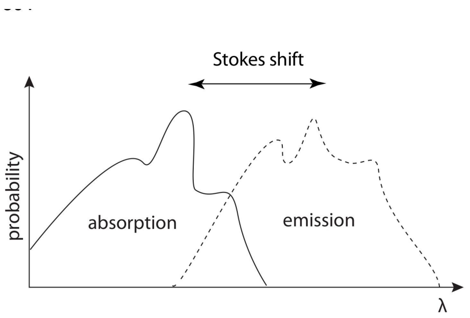

Figure 3.2: Schematic view of Stokes-Shift in organic scintillators [5]

To minimise the self absorption in the scintillator, the Stokes shift of the material should be as big as possible. This means the scintillator has to be transparent for the emitted photons. The scintillator light can then be detected for example by a silicon photomultiplier (SiPM), which is explained in subsection 3.3. The scintillator light has usually a too small wavelength to be detected directly by a SiPM. This is where a wavelength shifting fibre comes in handy, which is explained in the following section.

3.2. Wavelength Shifting Fibres

A wavelength shifting (WLS) fibre is a fibre which is commonly used in combination with scintillators and SiPMs to overcome the problem of the not compatible wavelength regions of the scintillator and SiPM. The WLS fibre absorbs the light from the scintillator and emits a photon with a larger wavelength due to the Stokes-Shift of the WLS fibre. The emitted light is isotropic and can travel to the end of the WLS fibre, where a readout happens [5]. The WLS fibre can be placed inside the scintillator (see section 5). Using the WLS fibre inside the scintillator in addition to the scintillator has another advantage. It increases the light yield at the SiPM as the WLS fibre is directly pointing at the SiPM.

3.3. Silicon Photomultiplier

A Silicon Photomultiplier (SiPM) is a semiconducting photon detection device. It receives a photon signal and converts it into an electrical signal due to the photoelectric effect. A SiPM is an array of Avalanche-Photodiodes connected in parallel on a shared silicon substrate. Therefore, multiple photons at once can be registered. An Avalanche-Photodiode consists of differently doped semi-conducting parts, which are connected to a bias voltage as seen in Figure 3.3 (a).

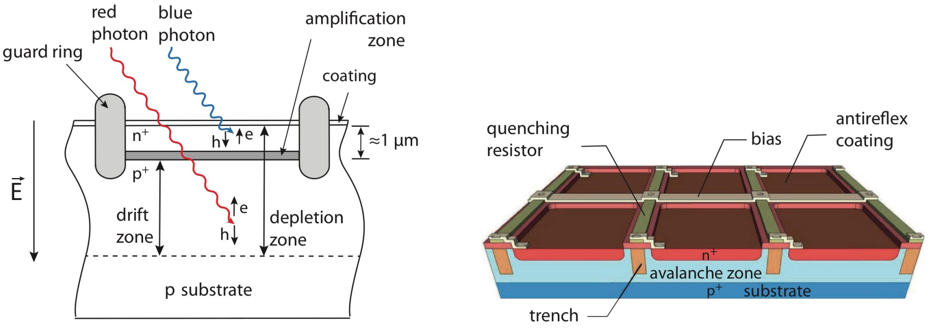

(a) SiPM cell.

(b) SiPM array.

Figure 3.3: Schematic of a SiPM [5]

The differently doped silicon build a diode. Using a reverse biasing of the diode a rather large depletion zone is created. The photon is absorbed and converted to an electron due to the photoelectric effect in the depletion zone. The depletion zone mostly extends into the p-doped area and is connected to the bias voltage. Due to the electric field of the bias voltage in the depletion zone, the created electron drifts towards a so called amplification zone, which is n-doped. There, a high electric field creates an avalanche amplification of the electron. The highly amplified electrons induce a signal on the collection electrodes, which can be read out. The breakdown voltage V_{BD} of a SiPM is defined as the bias voltage V_{Bias} where the electric field is strong enough to create an avalanche. Therefore, the bias voltage defines the amplification of the SiPM. The difference of those two is defined as the over voltage $\Delta V = V_{Bias} - V_{BD}$. The height of the signal from the SiPM is proportional to the number of hit pixels in the SiPM which is the same as the number of photons it receives.

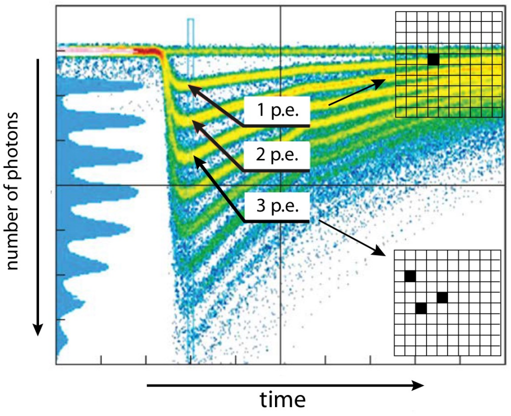

Figure 3.4: Signal Shape of the SiPM output (Photopeaks) corresponding to number of hit Pixels [5]

The number of hit pixels can then be seen as the signal heights in Figure 3.4. That are the so called photoelectronpeaks [5]. The amplitude of a signal coming from an SiPM is usually given in numbers of photoelectrons 'pe'.

3.4. Coincidence Measurements

Measuring particles via time coincidence is a commonly used technique in particle physics. It is used as it is helpful in suppressing noise signals, because the simultaneous occurrence of two independent signals is rare. The simultaneous occurrence of two signals can be proved with this method. Considering one particle passing through two detectors, a signal in both of them within a certain time window proves the occurrence of the processes happened simultaneously within the time window via coincidence measurement. Meaning a particle has passed through both of the detectors. This can for example be done with two scintillators. This method can be generalised with any number of hits. In case of the main measurement of this thesis the coincidence of four scintillators is required.

When using the explained method one has to consider the possibility of accidental coincidences, meaning the occurrence of two uncorrelated background signals which occur independently and simultaneously in two scintillators and mimic a real coincidence signal. The rate of accidental coincidences N_{acc} can be calculated

$$N_{acc} = \sigma \cdot N_1 \cdot N_2 \tag{3.1}$$

where N_1 and N_2 are the single hit rates in each scintillator and σ the coincidence time window.

4. The SHADOWS Experiment

The SHADOWS (Search for Hidden And Dark Objects With the SPS) experiment [3] is a proposed experiment to search for new physics. It aims to find Feebly Interacting Particles using a 400 GeV proton beam colliding with a beam-dump. As explained in subsection 2.3, FIPs are a promising candidate in the search for new physics. When protons collide with a beam-dump a variety of particles is produced, but most of them are absorbed by the beam-dump, except muons, neutrinos and FIPs. In addition, a large number of low energy neutrons is created in the hadronic interactions and escape the dump. The goal of the SHADOWS experiment is to measure possible FIPs emerging from the beam-dump via their resulting decay products. For example the experiment could be sensitive to the measurement of a FIP decaying into a muon pair. FIPs can only be measured via their decay products. Therefore, it is essential to reduce the background as much as possible and to know its composition to minimise misidentification of decay products with background particles emerging from the beam-dump. Therefore, studying the background flux with simulations as well as measuring the background flux is very important. This chapter gives an overview of the facility, the detector concept of SHADOWS and the background studies.

4.1. Experimental Area at CERN

The SHADOWS experiment is planned to be located at the CERN North Area in the TCC8 tunnel upstream of the ECN3 experimental hall, which is connected to the Super Proton Synchrotron (SPS) via the K12 beam line. The SPS will serve the area with $2 \cdot 10^{13}$ 400 GeV protons per spill every 15 s with a spill duration of 4.8 s. The SPS is a particle accelerator, which is part of the accelerator complex at CERN. It can accelerate different particles and is mostly used to accelerate protons up to 400 GeV after receiving them already pre accelerated from the Proton Synchrotron (PS), a smaller synchrotron, which is also part of the CERN accelerator complex.

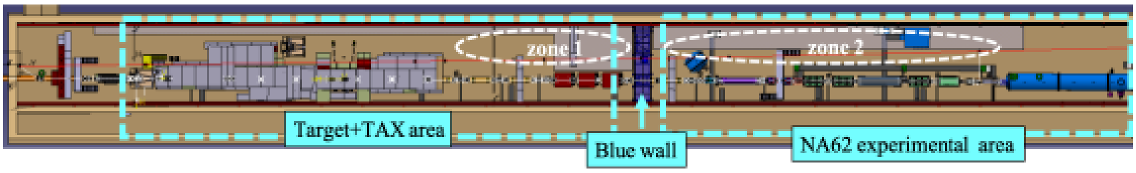

Figure 4.1: ECN3 Experimental Hall overview [3]

The area is separated into two parts. The target and TAX (Target Attenuator for eXperimental areas) area where the SHADOWS experiment will be placed on the left and the experimental area on the right in Figure 4.1. The coordinate system seen in Figure 4.2 is used throughout the whole thesis. The proton beam comes from the left. The coordinate z = 0 corresponds to the position of the beryllium T10 target. x = 0 and y = 0 correspond to the centre of the beam line in both directions, respectively. The SHADOWS detector will be placed in zone 1. The Target and TAX Area is seen in Figure 4.2.

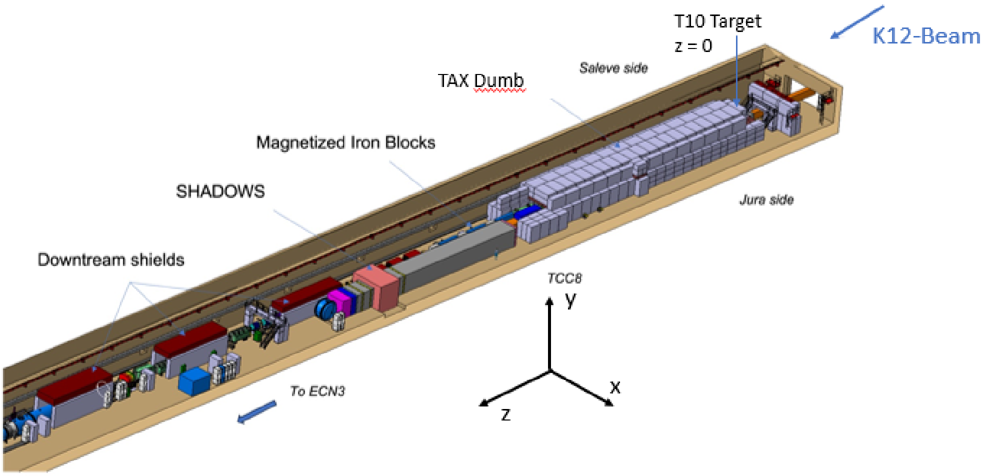

Figure 4.2: Target+TAX Area adapted from [3]

It consists of a beryllium target called T10 and a TAX, which is used as a beam-dump. The T10 is moved out of the way for SHADOWS and the copper-iron TAX is used as a beam-dump.

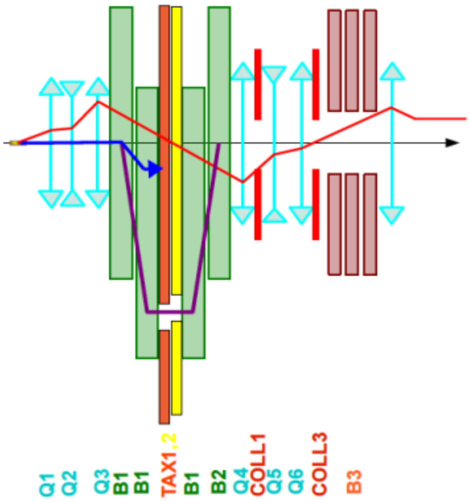

Figure 4.3: Beam schematics at the TAX in different Modes [3]. The blue line refers to the Proton Beam dumped at the beam-dump

The TAX seen in Figure 4.3 consists of two thick copper-iron blocks, red and yellow in Figure 4.3 which can be moved such that they form a hole or not. Therefore, the TAX can be used as a collimator for a beam as well as a beam-dump. In addition, to the moving TAX, magnets are used to bend a beam through the TAX hole when used as a collimator. For SHADOWS the B3 is a horizontal muon sweeper (x-direction) and the B1 and B2 magnets are used as vertical muon sweepers (y-direction) to remove as much muons as possible from the SHADOWS position. But some particles are still swept horizontally into the SHADOWS acceptance.

4.2. SHADOWS Detector

The proposed SHADOWS detector is going to be placed off axis around x = 1.5 m from the beam on the left side of the beam when looking downstream with a distance of $z \approx 38$ m to the T10 Target [3], which is 12 m upstream the beam-dump. The detector is planned to be 19 m long. The off-axis position of the detector reduces the total FIP yield reaching the detector, but it also decreases the background flux compared to an on-axis position.

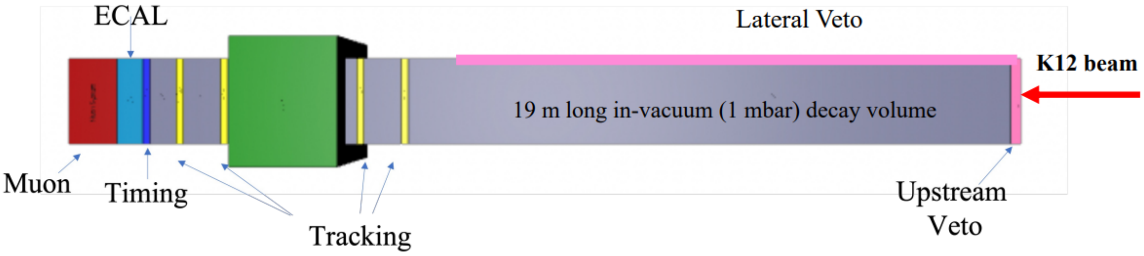

Figure 4.4: The SHADOWS detector [10]

The detector concept can be seen in Figure 4.4. The FIPs coming from the beam-dump are going to traverse the detector and decay e.g. into two muons in the decay volume. The decay products can be reconstructed to identify the FIPs. The SHADOWS detector is going to be reached by background muons as well as FIPs. Therefore, it is crucial to distinguish between background muons and muons emerging from a FIP decay.

To do so, the detector is proposed to consist of a Veto detector in front of the decay volume. As FIPs are Feebly Interacting particles they do not leave a track in the veto detector, background muons on the other hand leave a track. That means it can be reconstructed whether the muons originate from a FIP decay inside the decay volume or from background. The other parts of the detector coming after the decay volume are used to tag and reconstruct the particles emerging from a FIP decay. It is planned to consist of a tracking detector, a timing detector, an electromagnetic calorimeter and a muon system. The tracking detector will consist of four tracking stations and a dipole magnet which provides a vertical field in y-direction. Two tracking stations are located before and two after the magnet. With that the momentum and tracks of charged particles can be measured. This allows to reconstruct the decay vertex of the FIP decay as well as the FIP mass. The timing detector is crucial to match particles emerging from the same FIP decay via their timing and to reduce combinatorial background (this is explained in detail in subsection 4.3). Behind that an electromagnetic calorimeter (ECAL) follows to reconstruct possible neutral photon pairs emerging from a FIP decay, as they cannot be reconstructed from the tracker. The last part of the detector will be a muon system to identify muons produced from FIP decays and again distinguish them from combinatorial muon background.

4.3. Background Studies

When the proton beam is dumped at the TAX a variety of particles are produced, but most of them are immediately shielded by the TAX. The FIPs can pass the beam-dump and the resulting background flux after the beam-dump consists of muons, neutrinos and neutrons.

Neutrons are mainly a danger for electronics and mostly do not interact with any detector part except the ECAL, where they can be identified as background.

The muon background consists of two sources: Combinatorial background and background due to inelastic interactions with the decay vessel. Both can mimic a FIP signal and do therefore need to be as small as possible. Combinatorial background means that a random combination of a $\mu^-\mu^+$-pair enters the decay vessel and can be mistaken to come from a FIP decay. The expected total background muon flux from simulation at $z = 57$ m can be seen in Figure 4.5.

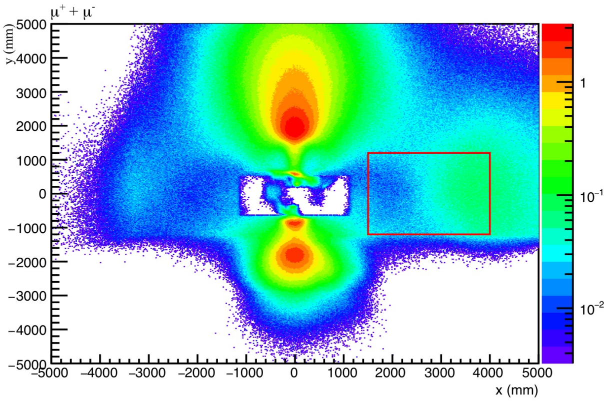

Figure 4.5: Simulated Muon Background at $z = 57$ m in front of the first SHADOWS tracking station [3]. The red box refers to the location of the SHADOWS detector.

The top part refers to positive muons and the bottom part to negative muons. They are bent in opposite directions due to the bending magnets in y-direction as described in subsection 4.1. To reduce the background muon flux at the SHADOWS position further, a Magnetised Iron Block system (MIB) system is planned as a muon sweeping system [3]. It is in principle a set of magnets which sweeps the muons out of the SHADOWS acceptance very efficiently while simultaneously shielding them and leading to the following simulated muon illumination.

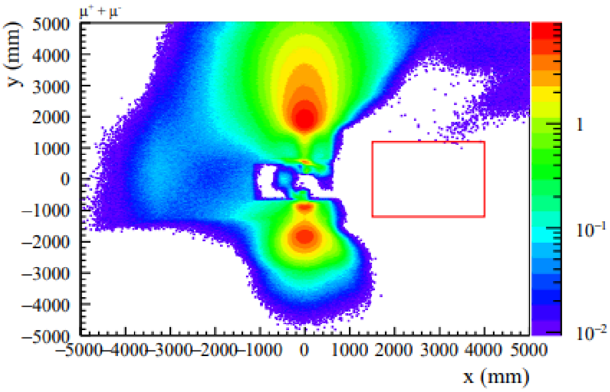

Figure 4.6: Simulated Muon Background in front of the first SHADOWS tracking station at $z = 57$ m with MIB[3]. The red box refers to the location of the SHADOWS detector.

As it can be seen in Figure 4.6 the muon background flux will be reduced by around a factor of 70 [3] due to the MIB. This leads to a lower combinatorial muon background. It is going to be reduced further by the usage of additional requirements in the single detector parts (see subsection 4.2).

The muon background due to interaction with the decay vessel happens when muons produced at the TAX enter the decay vessel and generate new particles while interacting with the decay vessel. Those particles can then decay further, mimic a signal and can be misidentified as a FIP.

Considering neutrinos a relevant background is due to inelastic interactions with the decay vessel, as they cannot be detected in any part of the detector. This would lead to similar resulting background particles as from the inelastic muon background. The contribution from neutrinos to the background is expected to be small [3]

The background muon flux emerging from the beam-dump and reaching the SHADOWS acceptance has to be studied further to minimise combinatorial background as well as background due to inelastic interaction. To validate the described simulations of the background muon flux a measurement of the background muon flux is performed and explained in section 6.

5. Muon Measurement Setup

The background muon flux at the proposed SHADOWS location is measured with this muon measurement setup. The absolute number of muons needs to be measured reliably with this setup. The idea is to use a simple but trustworthy and efficient detector design. In addition, to measuring the absolute number of muons the efficiency and acceptance needs to be known precisely. This is important to estimate the absolute muon rate from the measured muon rate. In this chapter the basic detector elements of the setup for the muon flux measurement and their testing are described.

5.1. General Setup

The muon measurement setup consists of a scintillator telescope as well as a silicon pixel telescope. The pixel telescope is added to the setup to perform a crosscheck of the scintillator part. Only the scintillator part is described in detail in this thesis. The design of the pixel telescope is described in [3] and [11].

The scintillator telescope consists of four plastic scintillator tiles made from BC408 by Bicron [12] with a size of 8.9 cm × 8.9 cm × 3 cm. The tiles are each containing two layers of wavelength-shifting fibres, which have 1 mm diameter and are made from Y10 by Kuaray [13]. They have a circular shape and both have the opportunity to be read out on both sides. In the end only one fibre on both sides is going to be read out.

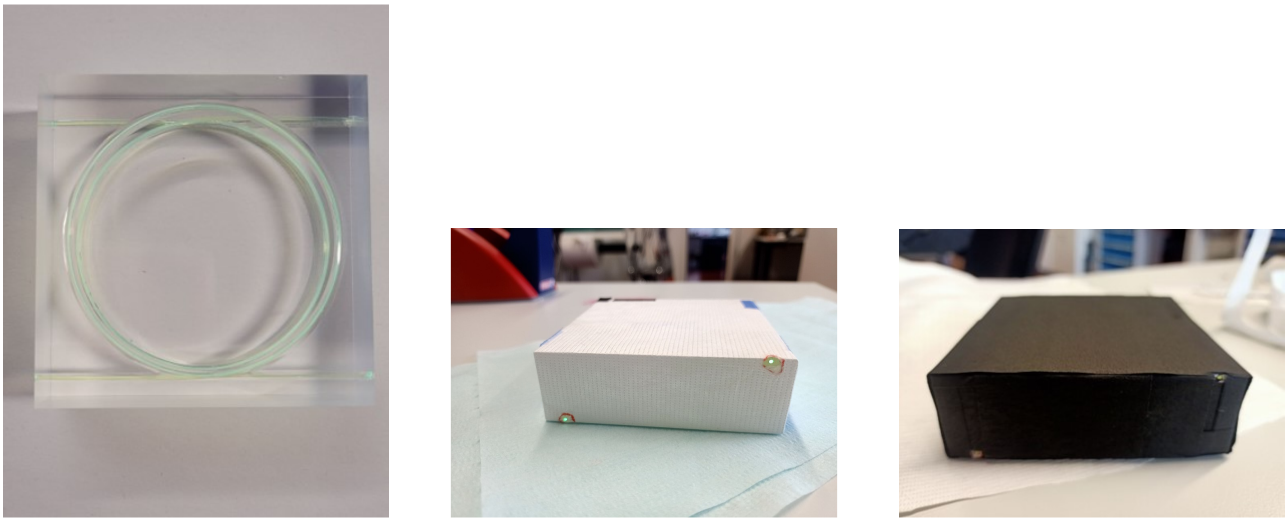

a) Scintillator Tiles with wavelength-shifting fibres inside

b) Wrapped with reflecting foil

c) Wrapped with light-tight tape

Figure 5.1: Process of Scintillator Tiles

The scintillators are wrapped with reflecting foil from Tyvek [14] as well as light shielding tape on top of that to maximise the light yield and to minimise noise induced by external light entering the scintillator. The different steps of the production of the scintillator tiles can be seen in Figure 5.1.

The final setup with four scintillator tiles can be seen in Figure 5.3. The scintillator tiles are sketched in green and are positioned with an equal distance between them. They are each connected on both ends of one WLS fibre to two single channel SiPMs with a size of 3 mm × 3 mm and a pixel size of 50 µm × 50 µm made by Hamamatsu S13360-3050CS [15] seen in Figure 5.2. When a particle traverses the scintillator it induces a scintillating light which is absorbed and emitted again by the WLS fibre which gives the emitted light the possibility to travel to the SiPM. This is explained in detail in section 3.

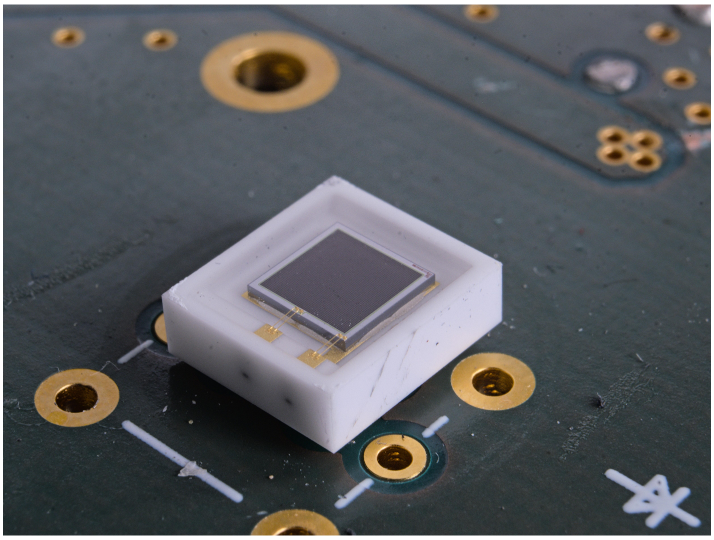

Figure 5.2: SiPM mounted on the Triggerboard

The SiPM is integrated on a Trigger Board and the signal is then readout by the Trigger Board, which can be seen in dark green in Figure 5.3.

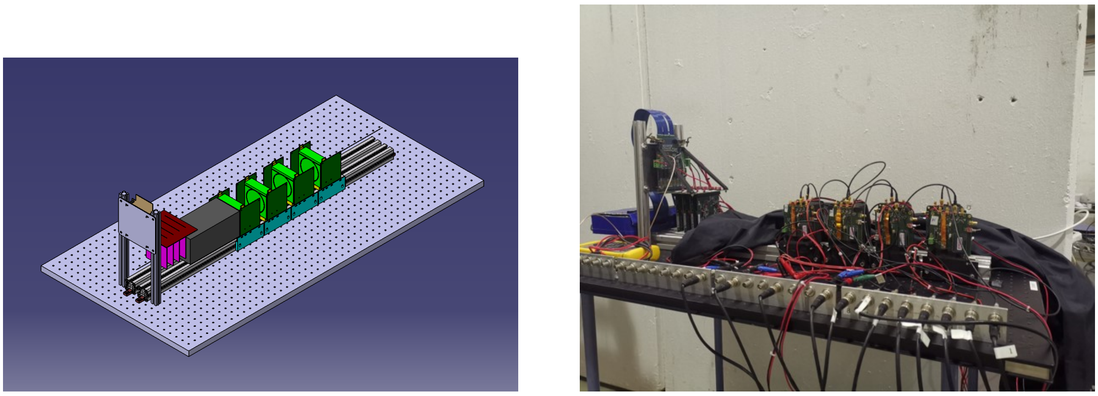

a) Schematic View of the Setup **b)** Real View of the Setup

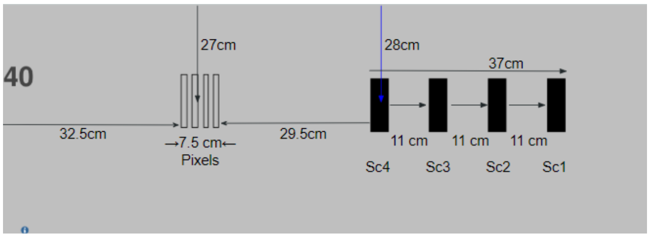

c) Dimensions of the Setup

Figure 5.3: Experimental Setup

The Trigger Board seen in Figure 5.4 is originally designed for a test measurement of the LHCb Scintillating Fibre Tracker [16] and is used again for the purpose of this measurement. It amplifies the SiPM signal and gives the opportunity to read out and process four different signals.

Figure 5.4: Top-View of the Trigger Board [17]

The electronic signal of the SiPM is amplified. This amplified signal can be directly accessed and measured. It is seen in Figure 5.7. The bias voltage of the SiPMs, responsible for the amplification of the SiPM as explained in subsection 3.3, can be adapted with a potentiometer on the Trigger Board. In addition, a tuneable threshold (th) can be applied to the signal. This gives access to the comperator signal. It gives a rectangular signal of constant height for the time duration of the amplifier overcoming the threshold. The buffer signal is a comperator signal with a constant time over threshold (ToT) and can be accessed. The ToT of the buffer signal can be adapted on the Trigger Board. Furthermore, a coincidence (AND) signal between the comperator or buffer and a signal coming from an external source can be accessed [17]. The circuit is visualised in Figure 5.5.

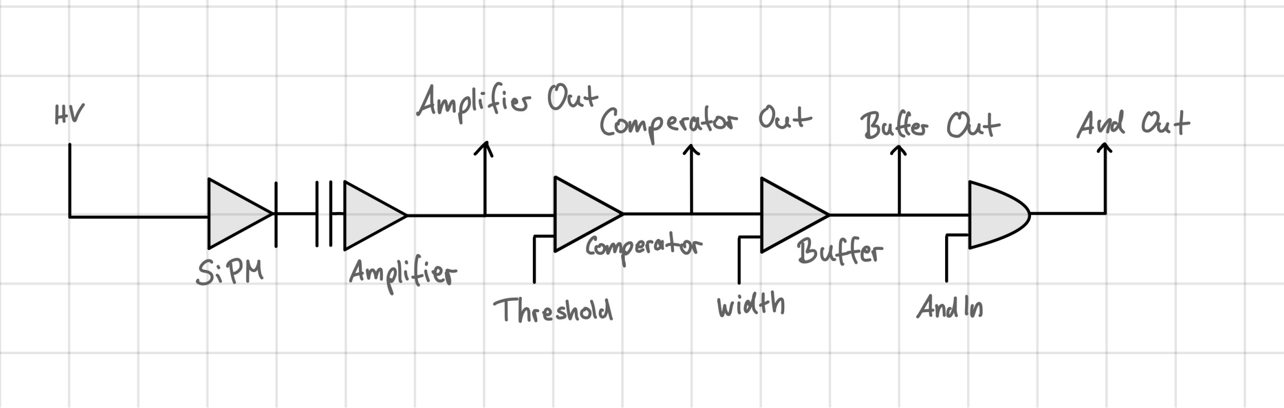

Figure 5.5: Schematic circuit of the readout of the Trigger Boards

The signals from the Trigger Board are then readout by an FPGA-based readout system, which records the number of the SiPM and timestamp (5 ns binning) of a hit.

As two Trigger Boards are connected to two outputs of one scintillator and there are four scintillators, they can be used to measure a coincidence in one scintillator as well as a coincidence in several scintillators as explained in subsection 3.4. The signals are readout independently and the coincidence is determined offline by matching the timestamps.

Furthermore, the setup has the capability to be used to determine the efficiency of each scintillator due to the usage of four scintillators including two readouts each at the same time. This is a useful feature to correct the measured data. This is used for the muon flux measurement and is explained in detail in subsection 6.4.

5.2. Readout Settings

The SiPM bias voltage is tuned such that all SiPMs have their first photopeak at a signal height of around 20 mV. This corresponds to a bias voltage of around 56 V in each SiPM. This implies an overvoltage of around 4 V [15]. These settings are chosen as they are recommend for the usage of this SiPM in combination with the Trigger Board [17]. For the measurements presented in this thesis the buffer signal of the Trigger Board is read out by the readout system. Using the buffer signal is useful to suppress unclear signals as well as afterpulses. If they occur in between the dead time of the buffer signal they are counted as one signal together with the original signal. The buffer length is set to 150 ns on all Trigger Boards. As afterpulses usually occur within 10 ns to 100 ns they are certainly suppressed with this.

To determine the best threshold for the measurement the signal dependence on the threshold is studied, which can be seen in Figure 5.6.

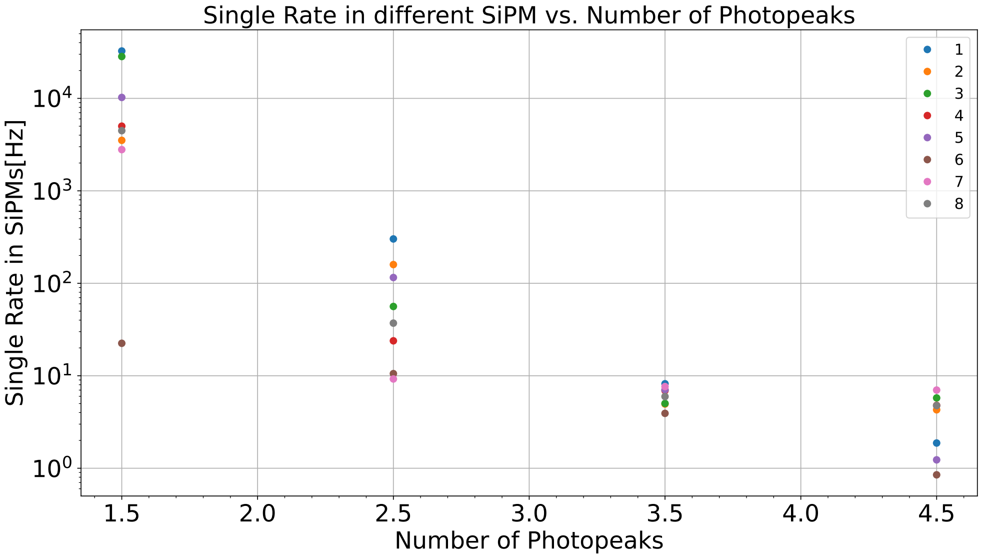

Figure 5.6: Single Count Rate dependence of the threshold expressed in terms of photoelectrons. The different marker correspond to the eight different SiPM used in the setup.

Therefore, a noise measurement is performed. The setup is placed in horizontal position to ensure reducing the acceptance of the setup to cosmic muons. The threshold is set to different values i.e. 1.5, 2.5, 3.5 and 4.5 photoelectrons and data is taken for all settings and all eight SiPMs, respectively. The results can be seen in Figure 5.6. As expected it can clearly be seen that the noise rate in all SiPMs decreases with threshold height. As muons induce a relatively high signal in the scintillator a high threshold does not cut them out, but reduces the noise rate dramatically. The different rate in each SiPM can be explained with slightly different threshold settings, different light leaks and hardware differences. But as this only influences noise it is negligible for the muon flux measurement.

After studying the behaviour of the rate of the SiPMs for different thresholds, the threshold is set to 4.5 photoelectrons where one photoelectron corresponds to around 20 mV. This can be seen in Figure 5.7. This threshold makes sure to suppress as much noise as possible while simultaneously keeping all muon signals. The signal height of a muon signal is studied with the oscilloscope. It is observed qualitatively on the oscilloscope and it can clearly be seen that the height of the muon signals is way above the 4.5 pe threshold. However, it is not possible to measure the height of the muon signal quantitatively with this setup. Therefore, the qualitatively observed height is used as an estimate. The reduction of noise with a higher threshold can be seen in Figure 5.8, in particular the occurrence of low noise signals is reduced by a higher threshold. The threshold settings are adjusted and studied using the Trigger Board while looking at the signal on the oscilloscope, which can be seen in Figure 5.8. To do this, the amplified signal is observed on the oscilloscope while the oscilloscopes trigger is set on the Buffer Signal. By adjusting the buffers threshold on the Trigger Board, the signals, which are detected, can be restricted. Therefore, the threshold is set to that value, when only signals above the 4th photopeak can be seen on the oscilloscope.

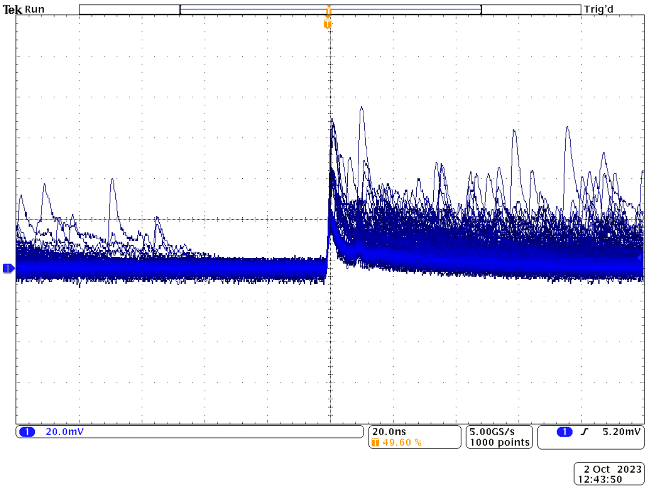

Figure 5.7: Amplifier Signal with different photopeaks visible on the oscilloscope

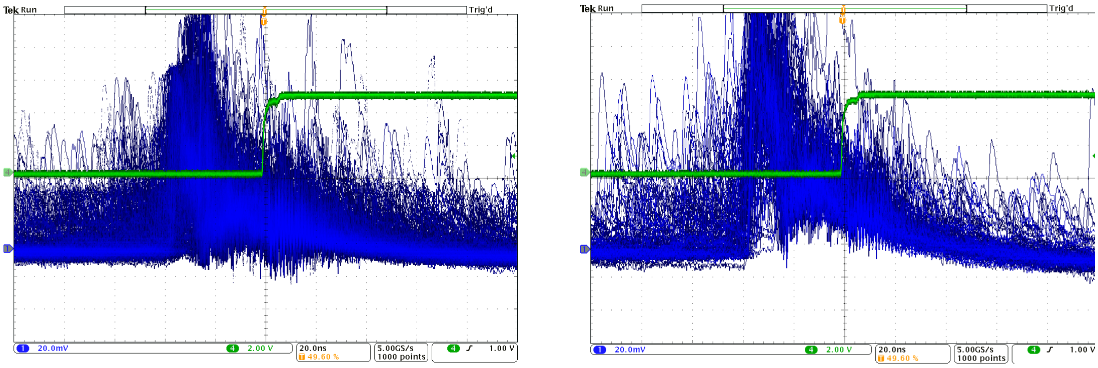

a) 1.5 pe threshold **b)** 2.5 pe threshold

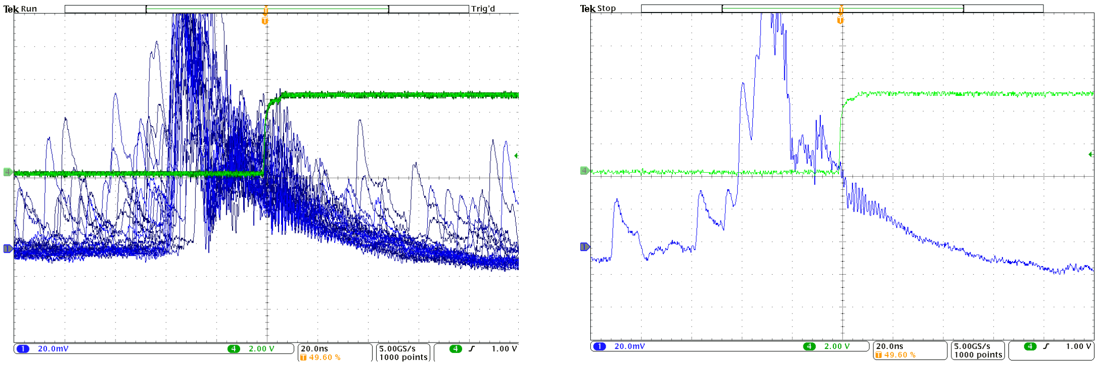

c) 3.5 pe threshold **d)** 4.5 pe threshold

Figure 5.8: Amplifier Signal (blue) at different thresholds seen on the oscilloscope while triggering on the buffer signal (green).

5.3. Test Measurements

To test and characterise the muon measurement setup for the background muon flux measurement, presented in the next chapter, test measurements are carried out, which are described in this chapter. The occurrence of afterpulses, the time resolution and the coincidence function are tested.

5.3.1. Afterpulses

Afterpulses can occur after a signal and can mimic an initial signal. Therefore, it is essential to study their occurrence and behaviour to reduce misidentification with an initial signal.

In case of SiPMs afterpulses can occur after a primary avalanche in a SiPM pixel when an electron is trapped in a pixel and is then released with a time delay and induces a secondary avalanche and therefore a signal. Afterpulses usually occur within a time window of 10 ns to 100 ns [18]. They can have amplitudes up to 1 pe. The released charge depends on the time difference between the original pulse and the afterpulse as well as the recovery state of the pixel.

The recovery state indicates whether the pixel is ready to fire again [19]. These afterpulses are studied using the data already described in subsection 5.2 within a time window of 100 ns for the 1.5 pe data set. The results are visualised in Figure 5.9.

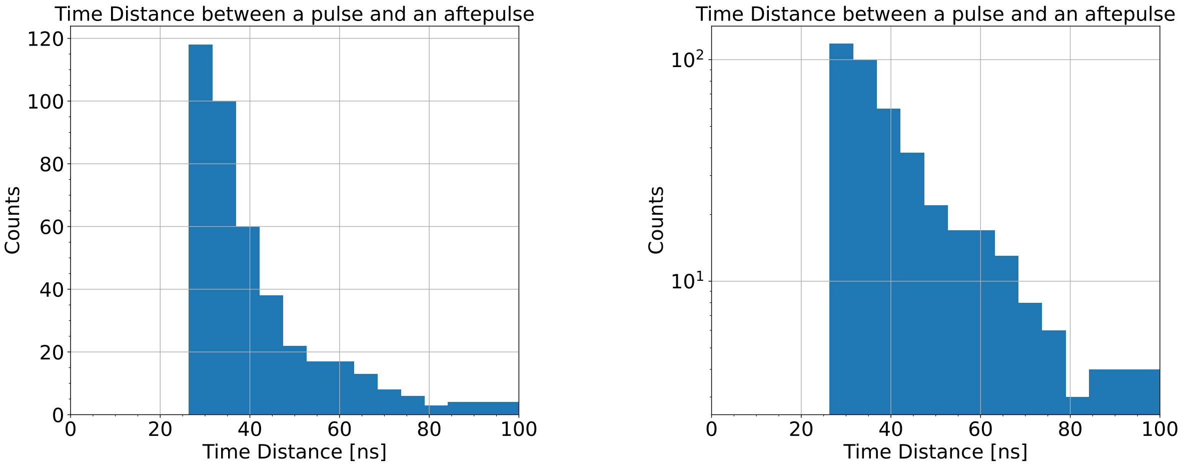

a) Linear Scale

b) Log Scale on the y-axis

Figure 5.9: Histogram of the Time Distance between a hit and an afterpulse for the 1.5 pe threshold data set

The occurrence of afterpulses starts after a time distance of around 25 ns. This delay is due to the usage of the comperator signal for this measurement. Since the typical time over threshold is 25 ns, afterpulses happening in this time window are sampled together with the initial photon signal. The number of found afterpulses decreases exponentially with a larger time distance to the original pulse and reaches a constant background for large time distances. This makes sense, as afterpulses are more likely to happen for a few tens of nanoseconds than for 100 ns after the initial pulse. The constant background, which is then left, consists of pulses which are within a certain time window of other pulses but are not afterpulses.

The same analysis is carried out with the data sets with a higher threshold but as expected no afterpulses are found due to the higher threshold. This does not mean there are no afterpulses, but it shows that they are not detected and do therefore not influence the measurement. This means that afterpulses will most likely not influence the measurement with the muon measurement setup as well, as the thresholds are set quite high as explained in subsection 5.2.

5.3.2. Time Resolution

The time resolution of the measurement setup can be restricted by different parts of the setup. To see which part of the muon measurement setup restricts the time resolution, a measurement of the time resolution of the different parts is carried out, respectively.

The time resolution is studied using a Time-to-Digital-Converter (TDC). To perform this measurement, two signals are sent to the TDC and the time difference between them is determined, evaluated and plotted in a histogram with a Gaussian fit to determine the standard deviation, which corresponds to the time resolution. This is done with two signals coming from a function generator to study the time resolution of the TDC, with two scintillating fibres positioned on top of each other to measure the time distance of a particle traversing both of them and connected to the known SiPMs and Trigger Boards used in the setup for the muon flux measurement as well as the original setup including one scintillator readout on both sides of the included WLS fibre each connected to a SiPMs. To generate hits the measurement is carried out while irradiating the setup with a ^{90}Sr source [1]. The signals coming from the function generator and the fibres are generated independently, where the signals coming from the scintillator are not. This is visualised in Figure 5.10. In case of the function generator, the TDC receives two independent but equal signals with a synchronised time distance from the function generator. In addition, the measurement of the scintillating fibres is carried out with two separated fibres as well. That leads to two independent signals reaching the TDC, respectively. Therefore, the time resolution of both cases can be calculated using the following formula, assuming it follows the Gaussian error propagation:

$$\sigma_{both} = \sqrt{\sigma^2_{single,1} + \sigma^2_{single,2}} \tag{5.1}$$

As $\sigma_{single,1}$ and $\sigma_{single,2}$ are the same the time resolution can be calculated with:

$$\sigma_{single} = \frac{1}{\sqrt{2}}\sigma_{both} \tag{5.2}$$

In case of the scintillator, the two read out signals are originating from the same hit in the same scintillator and are therefore correlated and not produced independently. For that reason the time resolution is not corrected by a factor of $\frac{1}{\sqrt{2}}$.

---

[1] ^{90}Sr is a β-source with a maximum energy of 0.55 MeV. It decays into ^{90}Y via the emission of an electron and an anti electron neutrino. ^{90}Y is a β-source with a maximum energy of 2.3 MeV. It decays into the stable ^{90}Zr via the emission of an electron and an anti electron neutrino.

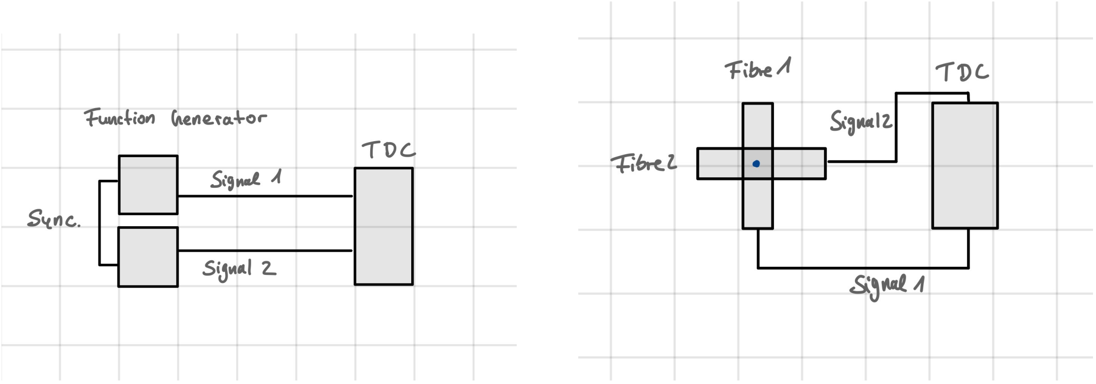

a) Two Signals from a Function Generator

b) Two different Scintillating Fibres

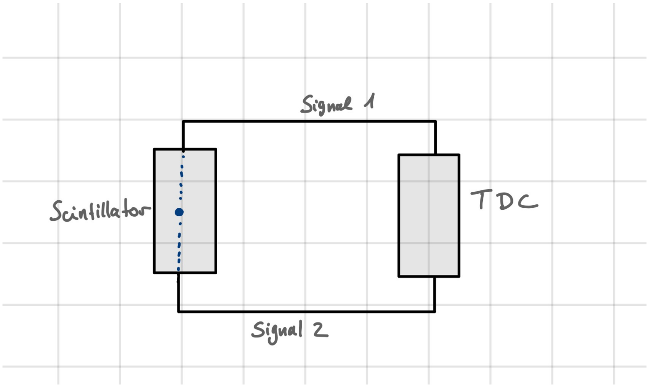

c) One Scintillator with Readout on both sides

Figure 5.10: Visualised Signal Path for the Time Resolution Measurement

The results can be seen in the following figures.

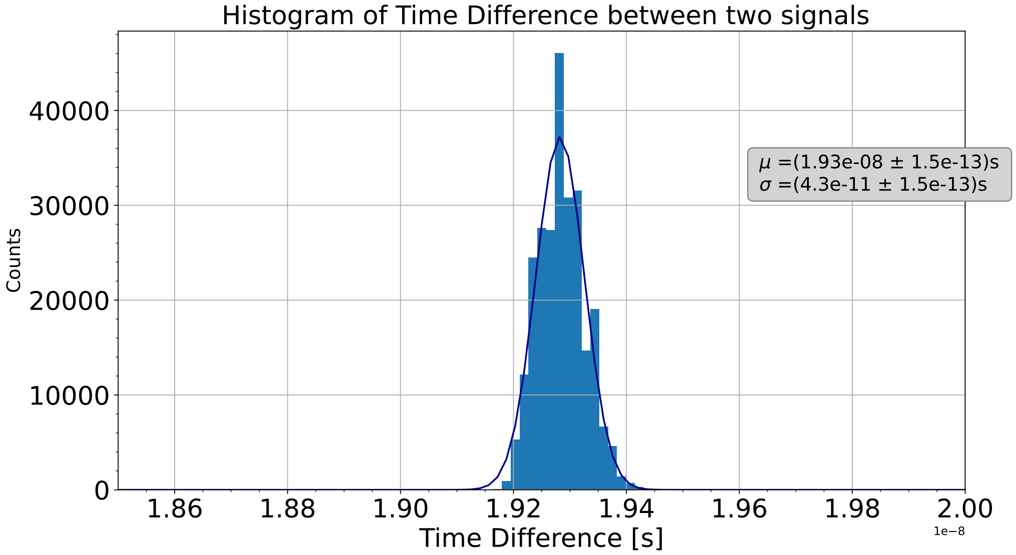

Figure 5.11: Histogram of the time difference of two signals of a function generator measured with the TDC fit with a Gaussian. The x-axis is given in 10^{-8} s.

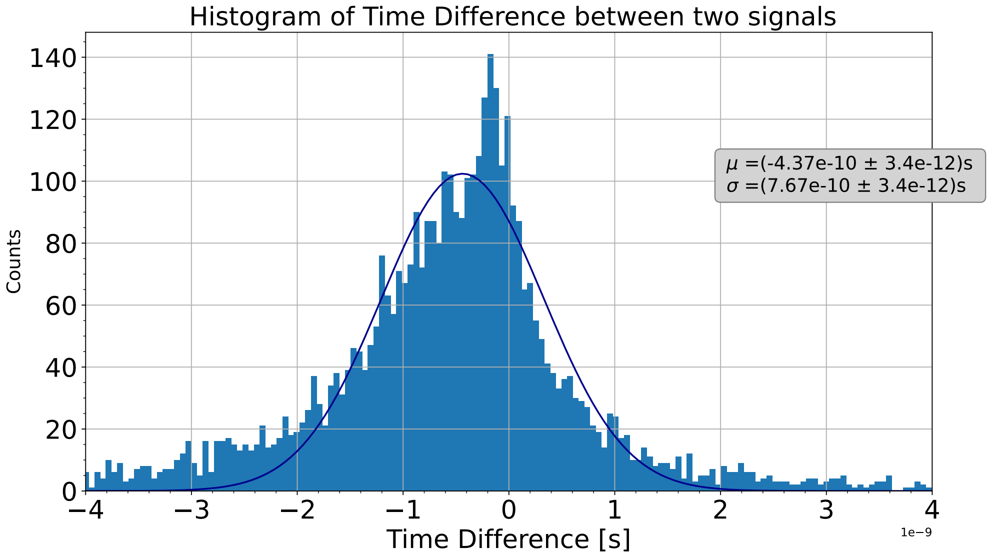

Figure 5.12: Histogram of the time difference of two hits in different scintillating fibres measured with the TDC at 4.5 pe threshold fit with a Gaussian. The x-axis is given in 10^{-9} s.

The histograms in Figure 5.11 and Figure 5.12 show the measured data, which is fit with a Gaussian, where the standard deviation corresponds to the time resolution of each setup. It can be seen that the distribution in Figure 5.12 is asymmetric. The origin of this is not completely understood. A possible solution could be electronic crosstalk, but this is not studied in the scope of this thesis. Therefore, the standard deviation is used to characterise the time resolution.

The measurement of the time resolution of the scintillator is carried out at a 4.5 pe threshold. The results of this measurement are shown in Figure 5.13. As the signals received from the two SiPMs are not generated independently in the scintillator, the determined time resolution is not divided by $\sqrt{2}$. It can be seen that the distribution in Figure 5.13 consists of a Gaussian with a standard deviation of the order of 1 ns as well as an additional Gaussian with a standard deviation of the order of 10 ps. To show this, the distribution is fit with a double Gaussian function. The origin of the second narrow peak is not completely understood, one possible solution could be electronic crosstalk, but this is not studied in the scope of this thesis. The standard deviation of the first broad Gaussian is therefore used to characterise the time resolution.

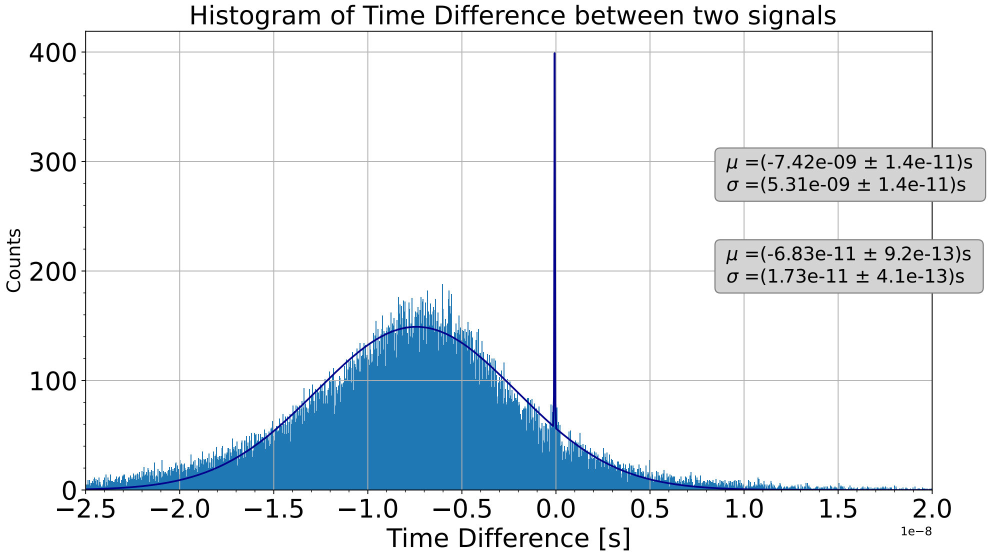

Figure 5.13: Histogram of the time difference of two hits in the same scintillator readout on both sides of the WLS fibre measured with the TDC with a 4.5 pe threshold fit with a double Gaussian. The x-axis is given in 10^{-8} s.

The results of the time resolution measurement are summarised in the following table.

Setup	Time Resolution σ
TDC	$(30.41 \pm 0.11) \cdot 10^{-12}$ s
Scintillating Fibres th = 4.5 pe	$(542.4 \pm 2.1) \cdot 10^{-12}$ s
Scintillator th = 4.5 pe	$(5.310 \pm 0.014) \cdot 10^{-9}$ s

Table 5.1: Time Resolution of the different Setups

Since the time resolution of the TDC and scintillating fibres are 2 or 1 orders of magnitude smaller than the scintillator, it can be assumed that their contribution to the time resolution of the scintillator blocks is negligible.

5.3.3. Coincidence Test

During the development of the muon measurement setup, the coincidence between different scintillators and SiPMs is tested to check its functionality as well as characterise its behaviour.

The following data is taken with the settings explained in subsection 5.2 with a noise run performed in horizontal position in the lab with a coincidence window of 100 ns. When looking at the coincidence rate of two SiPMs connected to the same scintillator (a) compared to the rate in two SiPMs connected to different scintillators (b) seen in Figure 5.14, it is noticeable that the rate in case (a) is substantially higher than in case (b). One point in Figure 5.14 corresponds to the number of coincidence hits in one second.

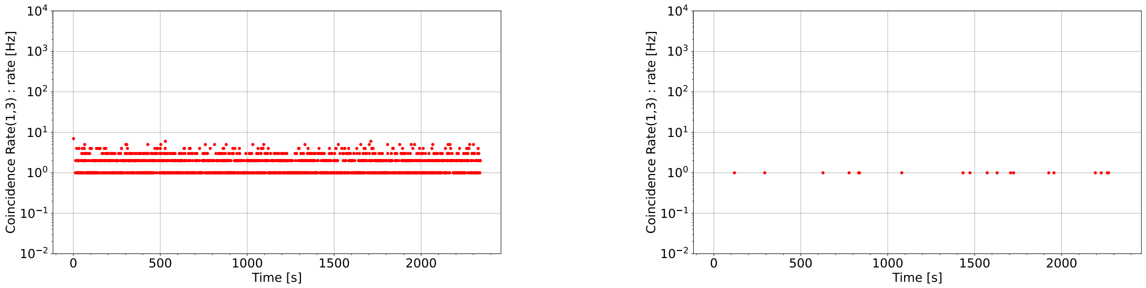

a) Coincidence Rate of two SiPMs in the same scintillator $f_c = 1.3$ Hz

b) Coincidence Rate of two SiPMs in different scintillators $f_c = 7.8$ mHz

Figure 5.14: Comparison of Coincidence Rate of two SiPMs for a noise run

This high coincidence in case of two SiPMs in the same scintillator cannot be explained with cosmic muons as the cosmic rate [2] even in vertical position is only $f_{cosmic} = 0.8$ Hz. Another crosscheck, which is performed, is the calculation of accidental coincidences as in subsection 3.4. It is determined to $f_{acc,a} = 1.4$ µHz and $f_{acc,b} = 2.3$ µHz. It can be seen that the rate of accidental coincidences does not influence the rate seen above.

As the SiPMs are read out on both ends of one WLS fibre, a possible explanation would be that a hit in SiPM 1 induces a hit in SiPM 2 as well, even if there is no hit in that one. In explanation, if a hit in SiPM 1 is recognised, an avalanche happens. In this avalanche UV-photons are produced which could be captured back into the WLS fibre and induce a hit in SiPM 2. This would lead to a too high rate of coincidences in one scintillator. To check this, the measurement is repeated with a readout of one SiPM connected to one fibre and the other SiPM connected to the other fibre which is also in the scintillator block. The results can be seen in Figure 5.15. One point in Figure 5.15 corresponds to the number of coincidence hits in one second. It is striking that the determined rate $f_c = 0.47$ Hz is significantly lower compared to the one for the readout of one fibre on both sides. This leads to the conclusion that the made hypothesis is correct and that the readout on both sides of one WLS fibre induces fake coincidence hits. The remaining number of coincidence hits can be assumed to be due to cosmic muons. As the measurement is done in horizontal position and the cosmic rate is lower in this case than in the calculated vertical case, this is in line with the determined vertical cosmic rate.

---

[2] As stated in subsection 2.2 the muon flux reaching the earth is $0.01\ \frac{\text{muons}}{\text{s}\cdot\text{cm}^2}$. Multiplying this with the scintillator area 79.21 cm^2 results in $f_{cosmic} = 0.8$ Hz.

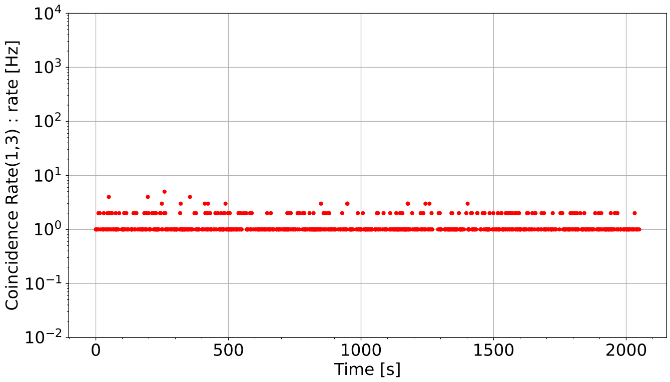

Figure 5.15: Coincidence Rate of two SiPMs connected to different WLS fibres in the same scintillator

The following measurement of the background muon flux is carried out with the readout of one WLS fibre on both ends. But the problem with the too high coincidence rate is considered and does not influence the determination of the background muon flux due to the characterisation of a muon. This means that due to the chosen muon criteria, the coincidence between two SiPM is supressed. This is explained in more detail in subsection 6.5.

It can be concluded from all the test measurements, that the setup works nicely and is suitable to measure the background muon flux.

6. SHADOWS Background Muon Flux Measurement

As explained in subsection 4.3 muons that pass the beam-dump and reach the measurement setup are a possible background source that might fake a FIP signal. Therefore, the background has been studied carefully by means of simulation as described in subsection 4.3. To validate these simulations a background muon flux measurement near the SHADOWS position is performed. In this chapter the general remarks of the facility important for this measurement are explained. Furthermore, the determination of the background muon flux in terms of number of muons per cm^2 per 10^{12} protons on target (POT) is described step by step resulting in the final number.

6.1. Current Experimental Area at CERN

The SHADOWS detector is planned to operate in the TCC8 tunnel upstream of the ECN3 experimental hall, where the muon flux measurement is performed as described in subsection 4.1. The ECN3 area is currently used by the NA62 experiment [20]. Therefore, the area has some different characteristics at the moment which are relevant for this measurement compared to what is explained in subsection 4.1. The SPS currently serves the area with $3 \cdot 10^{12}$ protons per spill every 15 s, with a spill duration of 4.8 s. The number of protons reaching the target or beam-dump each spill is called Protons on Target (POT) and is provided for every spill reaching the beam-dump.

The facility can be used in two different modes at the moment. In the case of this measurement: The so called "NA62-Mode" and the "SHADOWS-Muon-Mode". The NA62-Mode is used to create a Kaon Beam. For that protons are sent on a beryllium target (T10) to study Kaon physics with the NA62 experiment [20], while the protons are dumped at the beam-dump in SHADOWS-Muon-Mode. The SHADOWS-Muon-Mode is nearly the same as the SHADOWS-Mode for the future operation of SHADOWS explained in subsection 4.1 except that the B3 magnet seen in Figure 4.3 is turned off and the MIB is not installed yet. In NA62-Mode the magnets B1 and B2 are used as bending magnets in y-direction to bend the kaon beam through the TAX-hole (see Figure 4.3). B3 is used as a horizontal muon sweeper in x-direction. That means positive muons are swept to the left in the acceptance of our measurement and negative muons to the right when looking downstream. The simulated muon illumination near the measurement position with the current settings can be seen in the following figure:

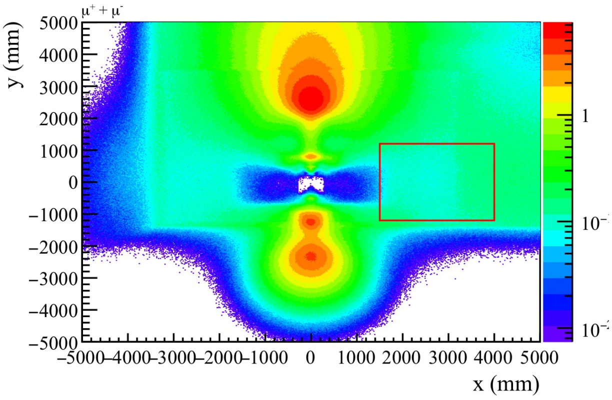

Figure 6.1: Simulated Muon illumination at z = 66.080 m (our measurement setup is placed at z = 72.68 m) with respect to T10. The red box corresponds to the xy-area where the muon measurement setup is placed [3].

6.2. Setup Position

The measurement setup to measure the muon flux is placed a few meters downstream from the future SHADOWS position seen in Figure 6.2 at z = 46.36 m with respect to the beam-dump, at positions x =(2.40, 2.93, 3.39) m, which corresponds to the names x = (beam, middle, wall) and the different x-position at which the measurement setup is placed and at y = -0.23 m, which is lower than the beam line. All these numbers assume the coordinate system introduced in subsection 4.1. The muon measurement setup can be seen in the following figure inside the red box. It is covered with a black cloth to shield it from light as much possible.

Figure 6.2: Muon Measurement Setup in the ECN3 Experimental Hall. The red box corresponds to the muon measurement setup.

The measurement is done at three different distances from the beam line to study the dependence of the muon flux from the distance to the beam. To allow the muons to pass the measurement setup without an angle and to achieve maximal acceptance the measurement setup is tilted differently for each of the positions. The angle α is derived using the following geometrical sketch in Figure 6.3, where x is the distance of the measurement setup to the beam line, and z the distance of the measurement setup to the beam-dump. Due to the large distance from the beam-dump, the angle α deviates only very little $(3.0, 3.6, 4.2)^\circ$ from 90 ° for the different positions, respectively.

$$tan(\alpha) = \frac{z}{x} \tag{6.1}$$

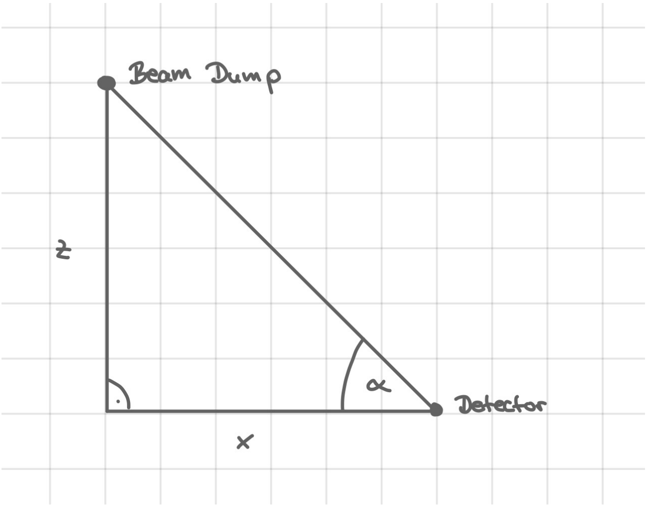

Figure 6.3: Geometrical Derivation of the Angle for the Setup Position

6.3. Measurement Settings

The measurement is carried out using the setup described in section 5 and the settings of subsection 5.2. As explained in subsection 5.2 the setup has a time binning of 5 ns and the buffer signal is read out with a threshold of 4.5 pe and a width of 150 ns. The data taking is separated into so called runs. Those runs do not have a specific time length or hit number, but all include a similar number of hits to keep them manageable for the analysis in terms of file size. In order to characterise the hits, an event is defined as the number of hits in a 100 ns time window which is also the coincidence window for the muon determination.

6.4. Efficiency and Acceptance

In order to correct the measured data for efficiency and acceptance, the efficiency for each individual scintillator is calculated using the recorded data. As the muons are determined by coincidence of the different scintillators, the efficiency is determined for the four individual scintillators and not for the eight SiPMs, respectively. Therefore, the idea is to characterise the efficiency of one scintillator by a hit in one of the two SiPMs located at the scintillator. That leads for example for the efficiency ϵ_1 of scintillator one to

$$\epsilon_1 = \frac{N((1 \vee 2) \wedge 3 \wedge 4 \wedge 5 \wedge 6 \wedge 7 \wedge 8)}{N(3 \wedge 4 \wedge 5 \wedge 6 \wedge 7 \wedge 8)} \tag{6.2}$$

where the numbers represent the eight SiPMs, where SiPM 1 and 2 are located at scintillator one and so on. N defines the corresponding number of hits. The efficiency is calculated by dividing the simultaneously occurring number of hits in all scintillators by the number of simultaneously occurring hits in all scintillators except scintillator one. As the efficiency for the scintillator and not for the SiPM is calculated, a hit in either SiPM 1 or 2 is demanded. The total efficiency to record a signal in all four scintillators is given by:

$$\epsilon_{tot} = \epsilon_1 \cdot \epsilon_2 \cdot \epsilon_3 \cdot \epsilon_4 \tag{6.3}$$

The efficiency determination is done for each run individually. Typical values for the scintillator efficiencies are given in Table 6.1.

Scintillator	Efficiency[%]
1	92
2	97
3	97
4	92
total	80

Table 6.1: Typical values for the scintillator efficiencies and the total efficiency

The efficiency defined in this way also considers geometrical acceptance effects, clearly indicated by the lower efficiencies of scintillator one and four. This can be explained by the geometry of the muon measurement setup: On the one hand to measure the efficiency of e.g. scintillator 2, events with hits in scintillator 1, 3 and 4 are selected. For these events the muons must also have passed scintillator 2 (see Figure 6.4). Therefore, if no hit is found in scintillator 2, this can only be explained by an inefficiency of the scintillator. On the other hand to measure the efficiency of e.g. scintillator 4, events with hits in scintillator 1, 2, and 3 are selected. For these events the muons must not have passed scintillator 4 as well (see Figure 6.4). Therefore, if no hit is found in scintillator 4, it could be explained by an inefficiency of the scintillator or by geometrical acceptance.

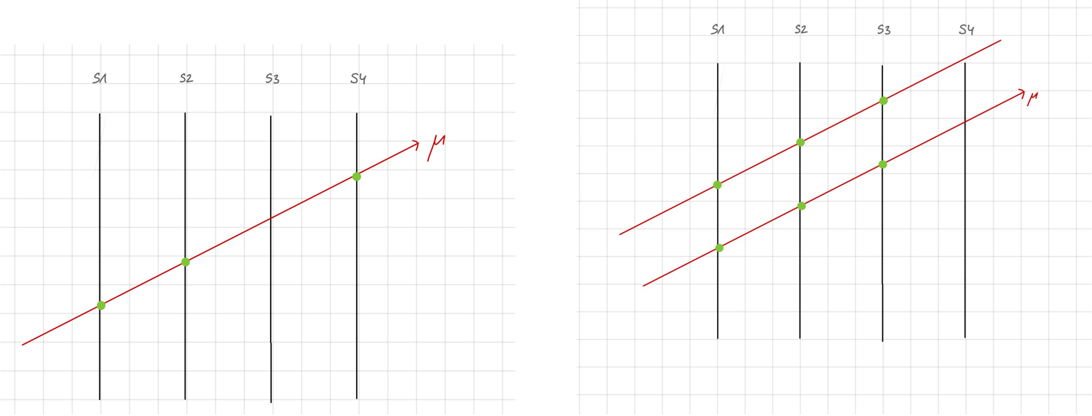

a) Inner Scintillator **b)** Outer Scintillator

Figure 6.4: Efficiency and Geometrical Acceptance Visualised

That leads to the conclusion that in this case a correction for efficiency already includes a correction for acceptance and an additional acceptance correction is not needed.

Furthermore, to validate this statement, a calculation of the expected acceptance loss due to the angular distribution of the muons for the fourth scintillator is carried out. The angular distribution of the muons is measured with the pixel telescope [11]. To be able to compare the result to the determined efficiencies, the probability of a muon hitting the fourth scintillator under the condition that the other three are also hit is determined keeping in mind the angular distribution. To do so the measured angular distribution of the muons from [11] is used as well as a geometrical derivation of the minimal and maximal angle of the muons passing the setup to still hit the fourth scintillator. It is determined to $P(4|1 \wedge 2 \wedge 3) = 0.94$. The analytical approach and calculation are explained in detail in Appendix A. Considering the efficiencies from Table 6.1 and assuming an inefficiency of the outer scintillators of 3 % as well, leaves us with $0.97 \cdot 0.94 = 0.91$ which matches the $\epsilon_4 = 0.92$ measured for the outer scintillator. Therefore, the measured acceptance loss of the outer scintillators is reasonable.

6.5. Muon Criteria

In order to determine the number of muons per cm^2 per 10^{12} POT from the data, a muon is characterised by at least one hit in each scintillator within a 100 ns time window. The selection is described as:

$$muon = (1 \vee 2) \wedge (3 \vee 4) \wedge (5 \vee 6) \wedge (7 \vee 8) \tag{6.4}$$

The numbers represent the eight different SiPMs, where SiPM 1 and 2 are located at scintillator one and so on. The number of muons defined by this criteria is determined for each spill and corrected for efficiency and acceptance individually for each run. To do so, the measured number of muons is divided by the determined total efficiency of that run. The number of POT is provided by CERN SPS for every spill. The goal is to compare the number of measured muons for every spill to the corresponding provided number of POT to get a normalised number of muons per POT. To do so, every measured number of muons for one spill can be matched via time to a provided number of POT for that spill. With that the number of muons is normalised to 10^{12} POT and divided by the scintillator area to get the number of muons per cm^2 per 10^{12} POT.

6.6. Time Resolution of the Measurement

Determining the time resolution of the measurement and the measurement setup is a good crosscheck for the time resolution of the setup determined in subsubsection 5.3.2.

Therefore, the time resolution of the measurement is determined using the measured data. This is done by extracting the time distance between two muon hits in the same scintillator and plotting it into a histogram. As the hits measured in the two SiPMs are originating from the same hit inside the scintillator, they are correlated and not produced independently. Therefore, the determined time resolution is not divided by $\sqrt{2}$. This is already explained in subsubsection 5.3.2 and is the same in this case. A Gaussian distribution is fitted to the data to extract the standard deviation seen in Figure 6.5. But the data is not described satisfactory by the fit. To get a better estimate of the time resolution the standard deviation of the distribution is calculated and used as an estimate for the time resolution.

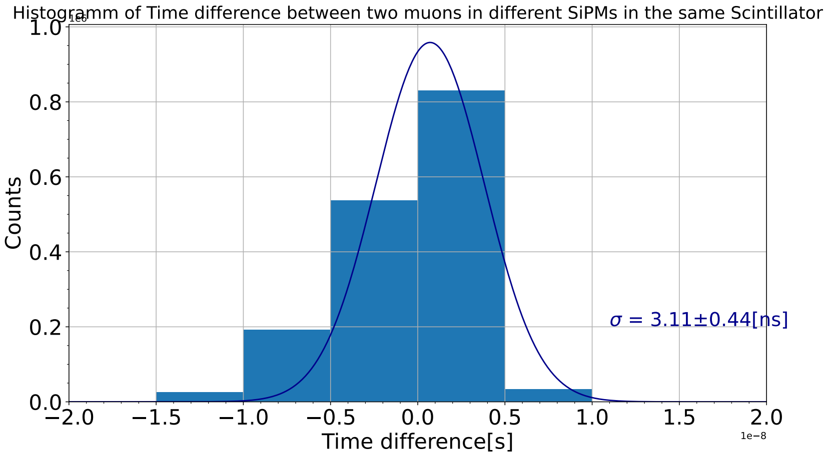

Figure 6.5: Histogram of Time Distance between two muon hits in the same scintillator fit with a Gaussian

Using the standard deviation of the distribution, it can be concluded that an estimate of the time resolution of the measurement is $\sigma_{meas} = 3.8\ ns$.

Having this result the time resolution of the setup can also be determined. To do so the error due to the time binning a of the readout system is calculated using [5]:

$$\sigma_{err} = \frac{a}{\sqrt{12}} = 1.4 \text{ ns} \tag{6.5}$$

The final time resolution of the setup can be derived to

$$\sigma_{set} = \sqrt{\sigma_{meas}^2 - \sigma_{err}^2} = 3.5\ ns \tag{6.6}$$

Comparing this to the time resolution determined in the lab, it is striking that the time resolution determined from the data is better than the one determined in the lab in subsubsection 5.3.2. A possible explanation could be the different energy characteristics of electrons from the β^--decay from the ^{90}Sr and the muons emerging from the beam-dump. As the muons have a higher energy than the electrons, they deposit more energy in the scintillator and induce a higher and faster flash than the electrons. Those can then be detected faster by the SiPM which would lead to a better time resolution. But this is not studied in the scope of this thesis.

6.7. Data Performance

While performing the measurement it is essential to have a look at the data and decide whether it is sensible and matches expectations. The data analysed in this section is taken in SHADOWS-Muon-Mode. First of all, the single hit rate in each scintillator is measured, as well as the coincidence rate of two SiPMs per cm^2 in one scintillator and finally the muon rate per cm^2.

Looking at the qualitatively performance of the single SiPMs in Figure 6.6 i. e. the single hit rate in each scintillator, it can be said that the spill structure is clearly visible compared to the noise rate in each scintillator and SiPM. Having a look at Figure 6.7 a constant background rate can be seen in all SiPMs as well as an additional higher hit rate every few seconds. This is the moment where a spill takes place.

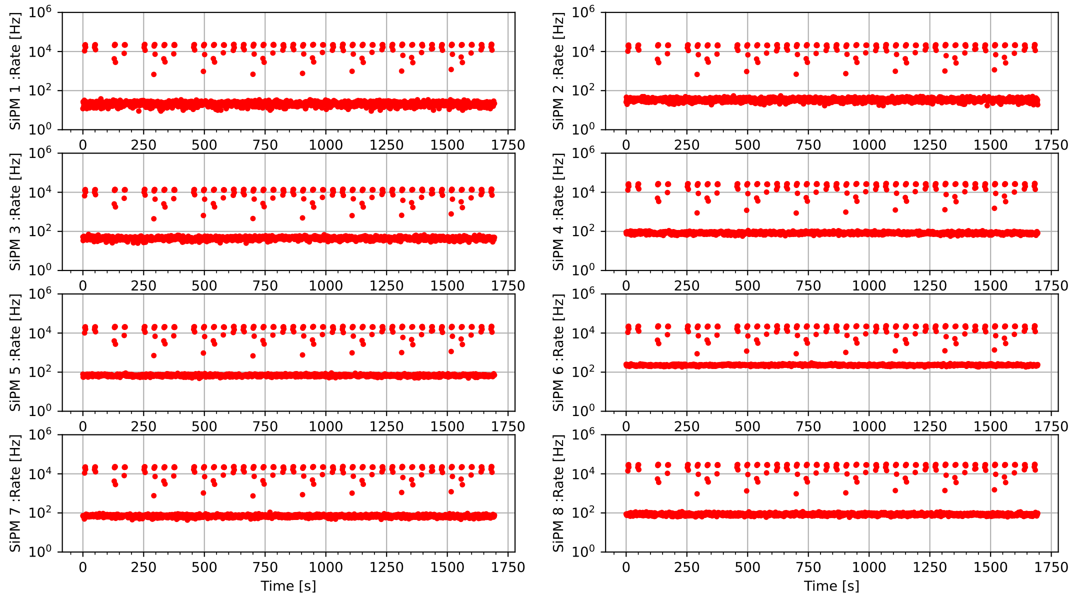

Figure 6.6: Single Rate of each SiPMs for one run.

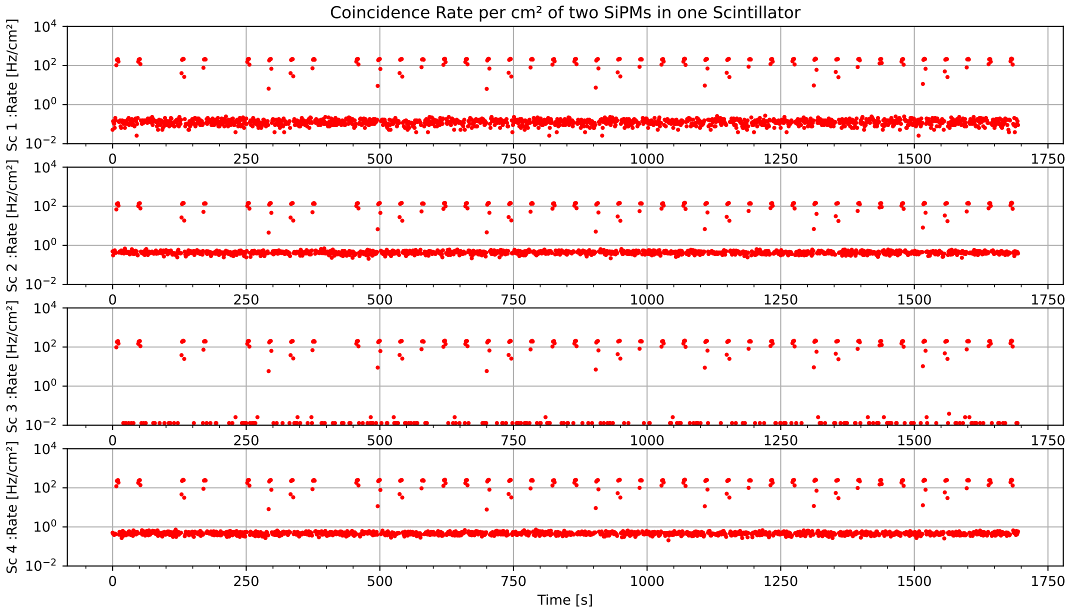

Figure 6.7: Coincidence Rate of two SiPMs in one Scintillator for one run

In addition, it can be seen from the coincidence rate of two SiPMs in one scintillator, that the noise rate in scintillator 3 is lower than in all the other ones. This is due to different contributions. First of all, a slightly higher threshold leads to a lower noise rate. Furthermore, a possible smaller light leak leads to a lower noise rate as well. The higher noise rates in the other scintillators does not influence the muon flux measurement as the noise rate completely vanishes after applying the muon criteria from subsection 6.5.

Looking at the total hit rate per cm^2 in all scintillators compared to the muon rate per cm^2 in Figure 6.8, shows that the noise completely vanishes in all scintillators after applying the muon criteria from subsection 6.5. This is due to the chosen muon criteria. As a muon is defined as a hit in at least one SiPM per scintillator (meaning at least one hit per scintillator) noise is suppressed, because it is very unlikely that four hits in different scintillators occur randomly at the same time. This is shown by calculating the rate of accidental coincidences for four hits. It results in $N_{acc}(4\ hits) \sim 10^{-9}$ Hz. Which shows that accidental coincidences are certainly suppressed compared to muons. Therefore, it is very reasonable that only muons are counted with this method.

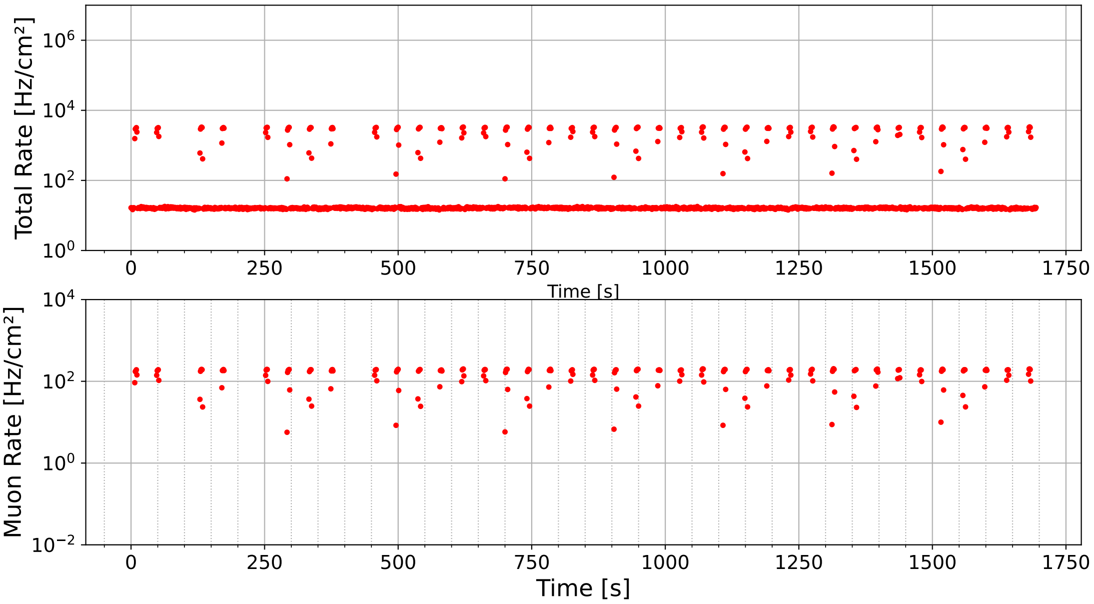

Figure 6.8: Total Rate in all Scintillators and Muon Rate in all Scintillators for one run

To make the explanation above more clear, the same plots are shown in the following figure zoomed in for a single spill.

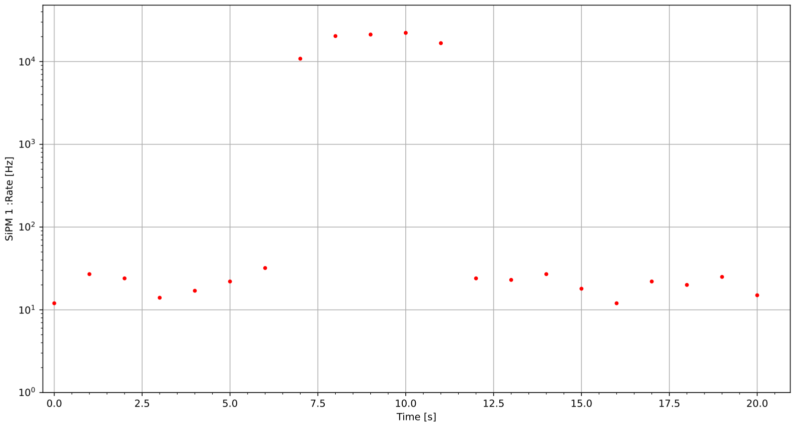

a) Single Rate in one SiPM

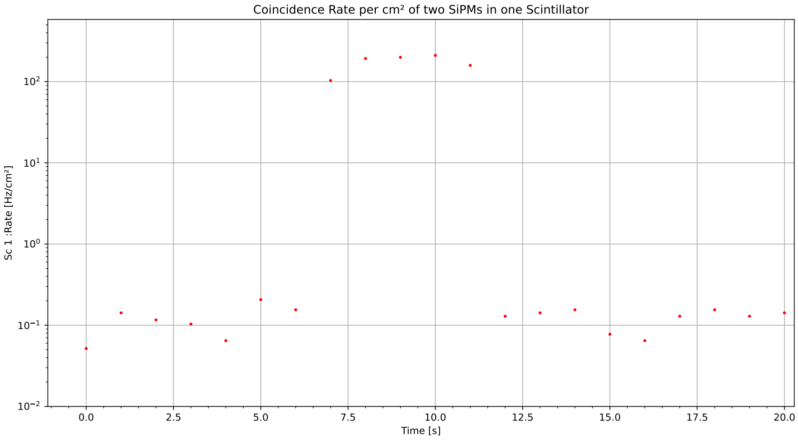

b) Coincidence Rate per cm^2 in one Scintillator

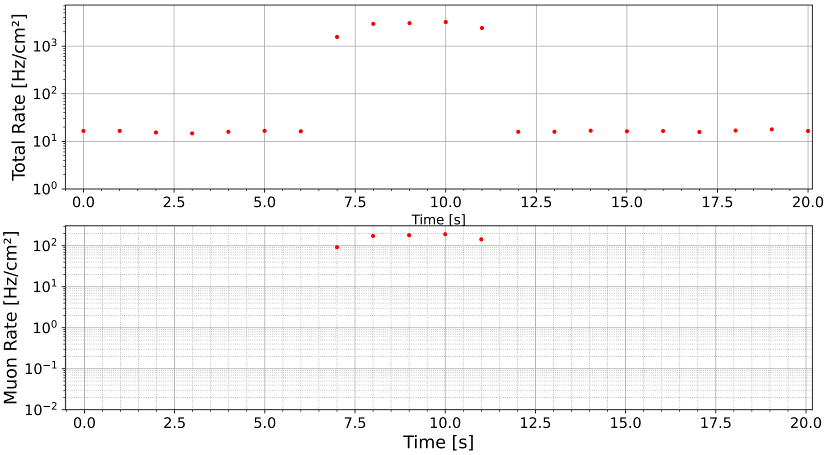

c) Total Rate and Muon Rate per cm^2

Figure 6.9: Different Rates visualised for a single spill

In addition, the number of SiPMs included in one event that means hit at least once in the 100 ns time window is studied.

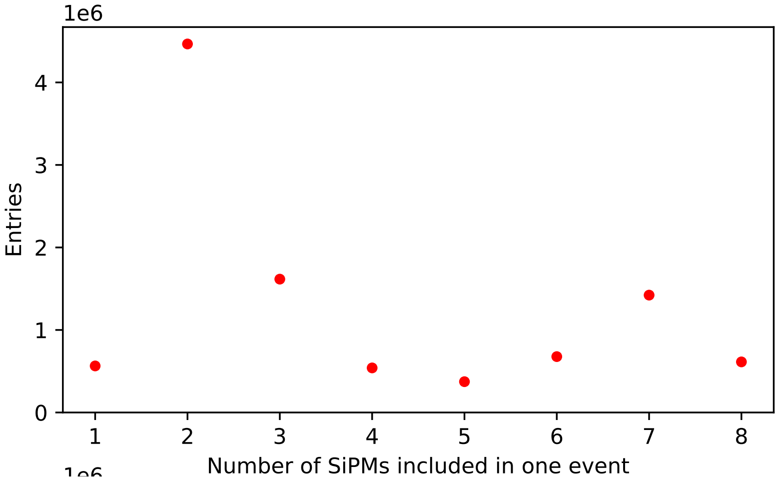

Figure 6.10: Number of SiPMs included in one event (hit at least once in 100 ns)

Looking at the above plot, one can make conclusions about the number of SiPMs included in one event. This can be useful to crosscheck, if the muon criteria is a good criteria to select the muons. Every entry is explained separately in the following. The events with only one SiPM can be assigned to noise hits. Even if noise can be clearly distinguished from real muons in Figure 6.8, it is sensible that all single noise hits add up to more events than all the muons, because the noise rate happens constantly and there are eight SiPMs contributing. The number of events with two hit SiPMs is striking. But referring to what is explained in subsubsection 5.3.3 and having a further look at the events contributing the most to that peak, it can be concluded that nearly all of those events are happening in one scintillator. This peak can therefore be explained with the problem of SiPMs sharing a WLS fibre and inducing each other a signal. The events with three or four SiPMs included can be assigned to muons not passing the whole detector due to geometrical acceptance or inefficient SiPMs. Considering the muon determination algorithm, the rising number of events with the number of included SiPMs larger than 5 can be assigned to the found muons. The reason for a rise of included SiPMs already at 5 included SiPMs and not 8, is that some SiPMs are inefficient or muons not passing through the whole measurement setup as explained in subsection 6.4. The drop between 7 and 8 included SiPMs in one event is studied further and it strikes out that the missing hit to achieve 8, in case of 7 hits in one event, is most of the time in scintillator 3. This is the scintillator which has the lower noise contribution due to a too high threshold explained earlier. Meaning that a muon with a lower energy is probably missed in scintillator 3 in this case. Therefore, this distribution seems reasonable and contributes to a reasonable event building and muon selection.

6.8. Muon Flux Determination

In this part the background muon flux is determined. Firstly, the data is checked for sensibility. Furthermore, the number of muons per POT per cm^2 is determined for each spill. The final number is determined by drawing a histogram of the number of muons per 10^{12} POT per cm^2 and fitting it with a Gaussian function. The mean value corresponds to the number of muons per 10^{12} POT per cm^2. It has to be said, that besides the scintillator data, data taken from the pixel telescope is used as well. The results are determined in the same way as for the scintillator data and can be found in [3] and [11].

The first step is to check whether the measured number of muons for each spill matches the number of POT of that spill. Each run is matched, using its timestamp, with the number of POT of that spill. One expects the number of muons to rise linearly with the total number of POT recorded, because more original particles result in a higher number of muons.

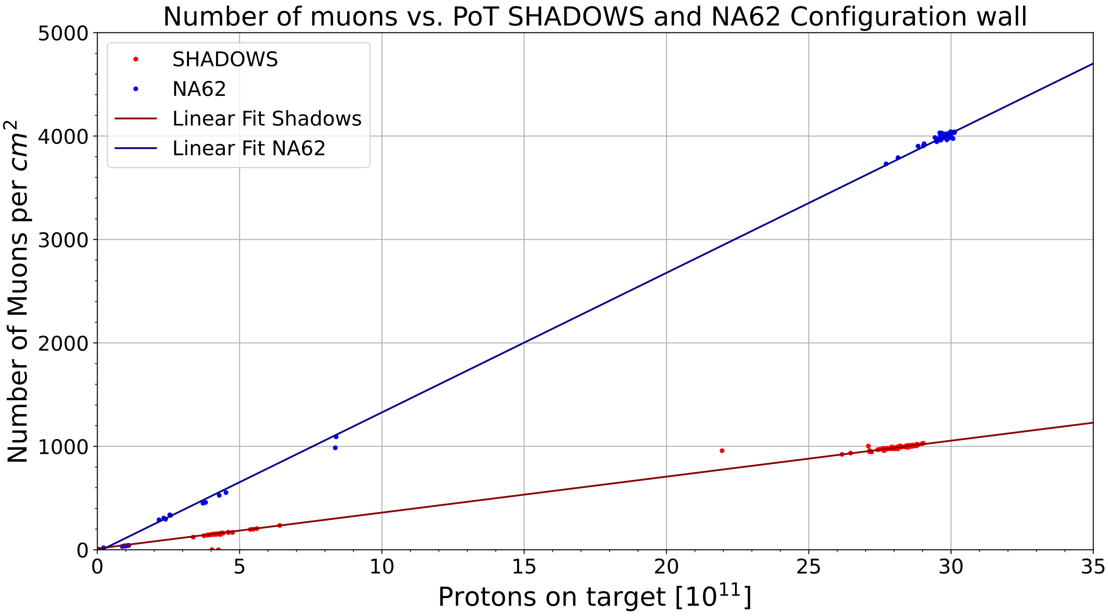

Figure 6.11: Number of muons vs. POT for different Beam Modes

There are two different data sets visible in Figure 6.11, one corresponding to the NA62-Mode and one corresponding to the SHADOWS-Muon-Mode. They are fit with a linear function. Therefore, it can be seen that the number of muons rises linearly with the number of protons on target. Furthermore, the number of muons per cm^2 per POT in NA62-Mode is constantly higher than in SHADOWS-Muon-Mode due to the different configuration of the magnets and therefore muons being swept directly into the position of the muon flux measurement as described in subsection 6.1.

To validate the taken data and the analysis the number of muons recorded as a function of POT is shown at the same time for data recorded with the scintillator and the pixel setup. In Figure 6.12 it can be seen that both agree well with each other and a linear behaviour can be observed. The two different data sets from the pixel and scintillator setup are located on top of each other in Figure 6.12. The correspondence between both data sets seems reasonable, as the data sets can be described by the same linear fit.

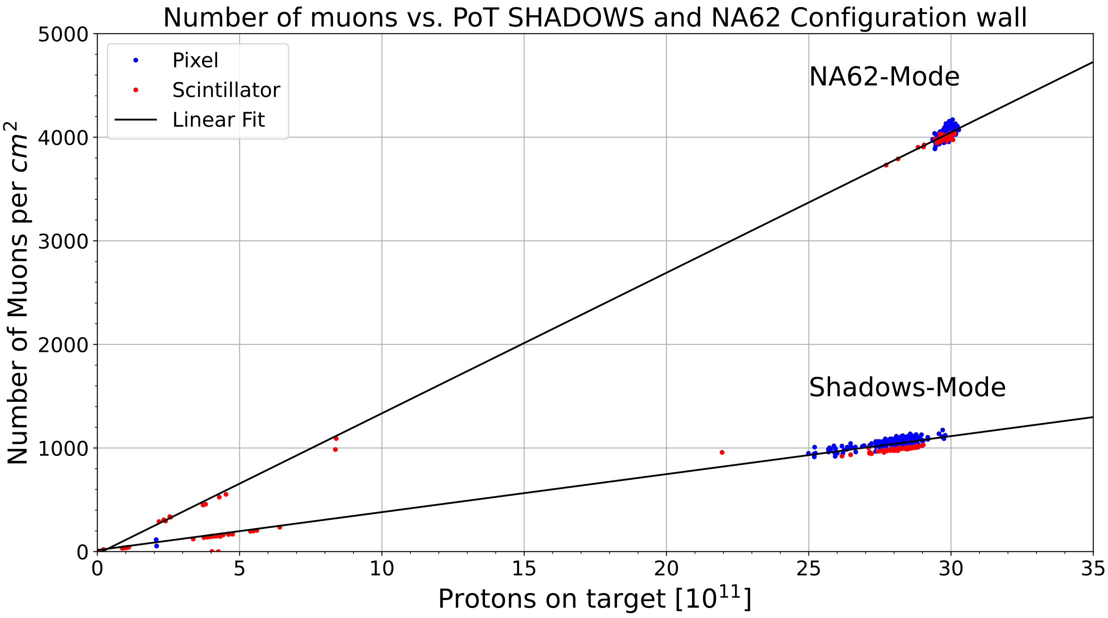

Figure 6.12: Number of muons vs. POT for different Beam Modes for Pixel and Scintillator Data

As explained in subsection 6.2 a measurement at different x-position of the setup is carried out to study the dependence of the muon flux on the x-distance to the beam line. The same analysis is carried out with the data taken in SHADOWS-Muon-Mode at different positions of the measurement setup seen in Figure 6.13. A linear rise for each distance to the beam line can be observed as before. The number of muons decreases getting closer to the beam.

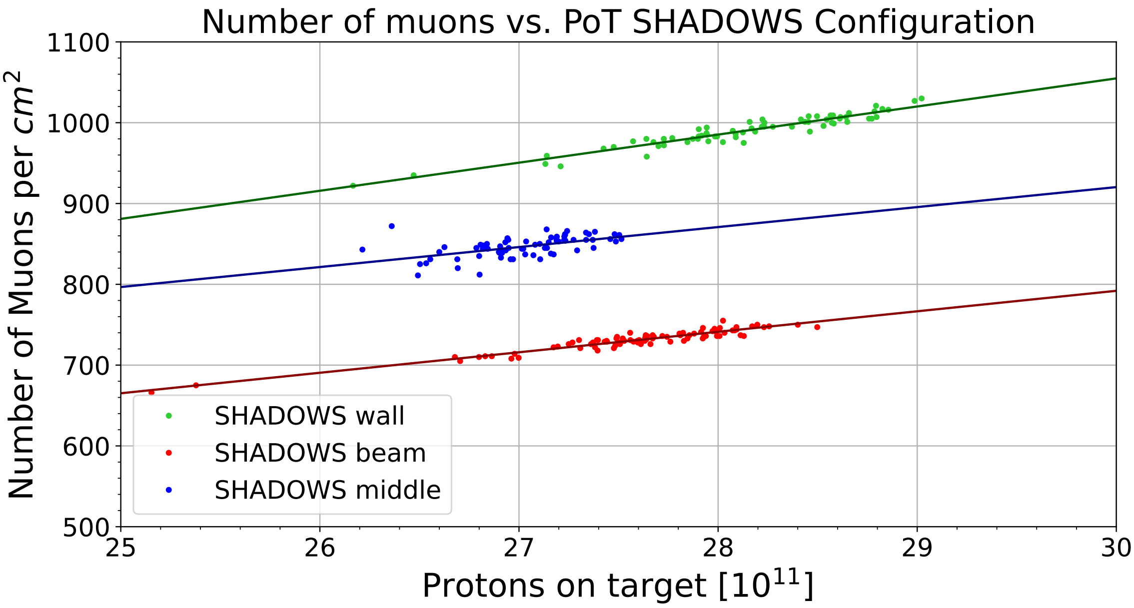

Figure 6.13: Number of muons vs. POT for different distances to the Beam Line in SHADOWS-Muon-Mode. The distance x = (beam, middle, wall) corresponds to x =(2.40, 2.93, 3.39) m

To get a final result for the number of muons per cm^2 per 10^{12} POT, the determined number of muons per cm^2 per 10^{12} POT for each spill is histogramed for the different configurations. The histograms are each fit with a Gaussian to determine mean μ and standard deviation σ and can be seen in Figure 6.14. This leads to one number of muons per cm^2 per 10^{12} POT for each configuration.

The standard deviation σ is used as the statistical error. The statistical errors are all around 1 % of the absolute value. As the error is the standard deviation of the Gaussian, it is a measure for the statistical spread of the determined absolute value over all the measured spills. Such low values suggest that all independently measured numbers of muons per spill agree quite well with each other.

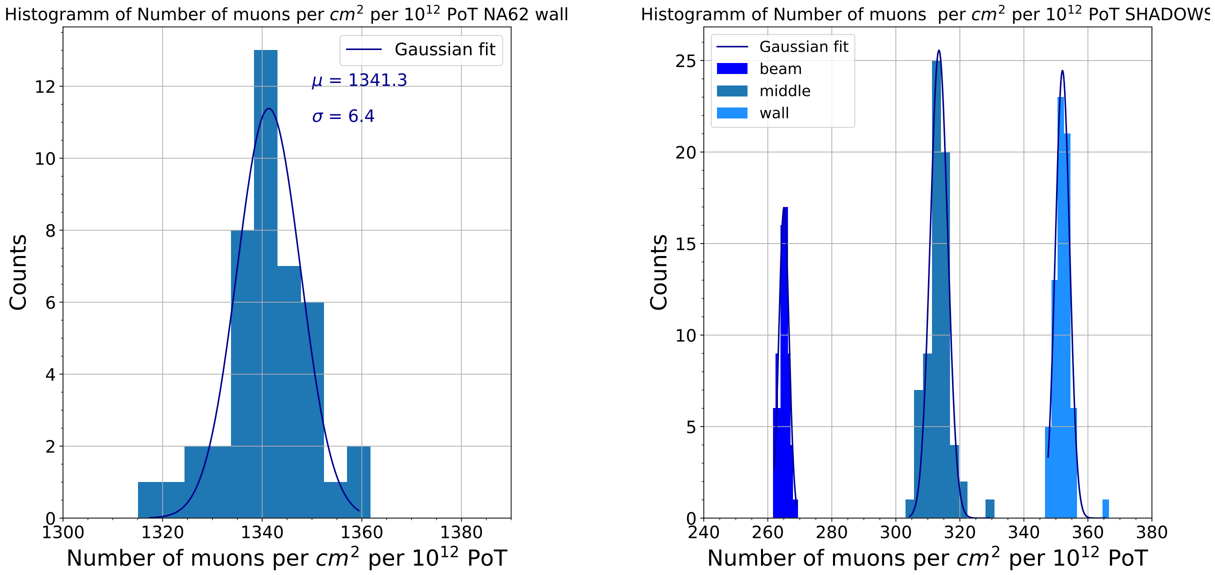

a) Number of muons per cm^2 per 10^{12} POT in NA62-Mode

b) Number of muons per cm^2 per 10^{12} POT in SHADOWS-Muon-Mode for different Positions of the Beam Line. The distance x = (beam, middle, wall) corresponds to x =(2.40, 2.93, 3.39) m

Figure 6.14: Number of muons per cm^2 per 10^{12} POT histogramed for different spills

Considering the systematic uncertainties, noise could be one possible source for a systematic uncertainty. But as explained and seen in Figure 6.8, noise is clearly suppressed with the used muon determination, because no muons are found in between the spills. Therefore, it can be neglected as a systematic uncertainty. Another systematic uncertainty could arise from edge effects in the scintillators. Meaning that the scintillator does not have the same efficiency over its whole area. This could for example arise from the position of the WLS fibre. Assuming the same nonuniform efficiency for all scintillators, respectively and considering that most muons pass the setup without an angle, leads to the conclusion that some muons could traverse the setup at the same inefficient position in each scintillator and are therefore not accounted for in the applied efficiency correction. But as the scintillator and pixel data agree quite well with each other this effect is probably small. Furthermore, another systematic error is certainly arising from the number of POT. The values are provided by CERN with a systematic error of 4 % [21]. It can be assumed that the systematic uncertainty of the measured POT has probably the largest influence on the systematic uncertainty, because a systematic wrong number of POT directly leads to a wrong number of muons per POT which is the number determined in this thesis. It can be said that the systematic uncertainty is larger than the statistical uncertainty. As the systematic uncertainty of the number of POT is considered as the systematic uncertainty, this is a characteristic of the measurement and not of the used setup in general. Therefore, this is considered and the results are summarised in the following table.

Configuration	Number of muons per cm^2 per 10^{12} POT
NA62 wall	1341 ± 6 (stat.) ± 57 (sys.)
SHADOWS wall	352.2 ± 2.2 (stat.) ± 14.1 (sys.)
SHADOWS middle	313.5 ± 2.7 (stat.) ± 12.6 (sys.)
SHADOWS beam	265.1 ± 1.6 (stat.) ± 10.6 (sys.)

Table 6.2: Muons per cm^2 per 10^{12} POT for different configurations. The distance x = (beam, middle, wall) corresponds to x =(2.40, 2.93, 3.39) m

The results for the different distances from the beam can be compared to the data measured with the pixel telescope [11] as well as the simulation data [22] (multiplied by three in Figure 6.15 [3]). The results of the pixel data are determined in a similar way. The results obtained for the different spills are fit by a Gaussian. The quoted values reflect the mean and standard deviation. The values are also corrected for efficiency and acceptance.

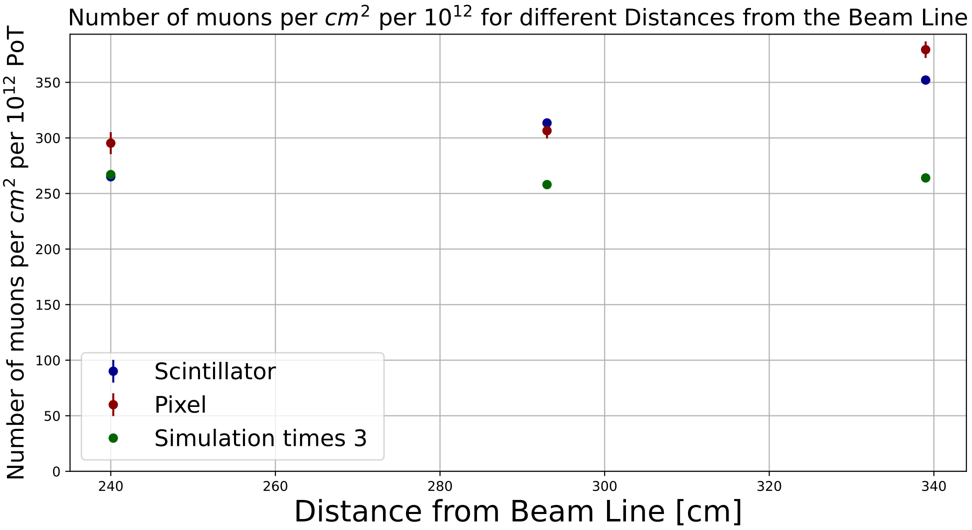

Figure 6.15: Number of muons per cm^2 per 10^{12} POT in SHADOWS-Mode with their corresponding statistical error vs. Distance to the Beam Line. The scintillator data point and the simulation for x = 240 cm can be seen on top of each other.

It is known from previous studies that the simulation underestimates the muon background arising from the beam-dump [3] and that the simulation matches the reality if it is multiplied by 3 or 4. Therefore, the simulation is scaled by three to compare it to the measured values.

With that the simulation is still constantly below the measured value. This matches the expectation of scaling it by 3-4. It can be concluded from this diagram that the scintillator and pixel measurement match each other, as well as the simulation given the expected discrepancy by a factor of 3-4. The only difference is that the simulation does not see a rise in muons while going further from the beam. This is the reason for the larger deviation of the data and the simulation for the last two data points in Figure 6.15. The pixel and scintillator setup as well as a third setup from another group [3] measured this effect independently. Therefore, it should be considered.

6.9. Measurement of the Soft Component of the Muon Spectrum

With the currently used measurement setup only the absolute number of muons per cm^2 per 10^{12} POT can be determined. But it would also be interesting to get an idea of the energies carried by the muons.

The setup has the option to include a 20 cm thick lead block to shield low energetic muons and study their fraction of the muon flux. This works because muons lose more energy the longer they travel through matter as explained in subsection 2.2. Meaning at some point while travelling through matter they have lost all their energy due to ionisation and are stopped. By comparing the muon rate with and without the lead block an estimate of the fraction of soft muons with momenta below a certain energy in the muon spectrum can be extracted. In Figure 6.16 the range of muons in lead is plotted against the muon energy.

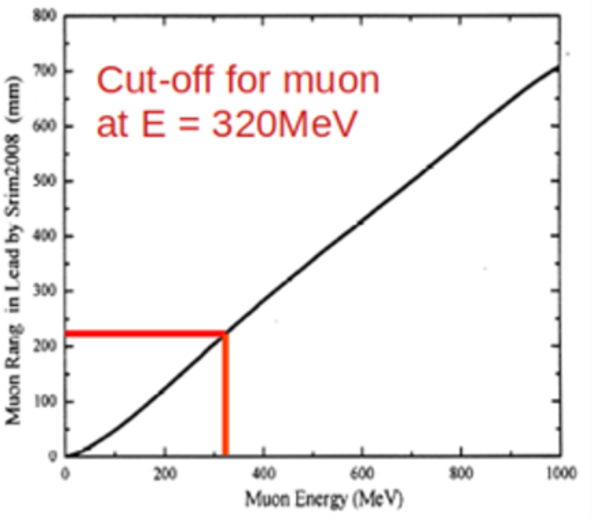

Figure 6.16: Muon Range in Lead depending on the Energy taken from [23, p. 7-12]

Therefore, it can be concluded from Figure 6.16 that the estimated cut off energy for muons passing the 20 cm lead block is around 320 MeV [23, p. 7-12].

In addition, multiple scattering of muons with the lead block has to be considered as well. Due to that muons are deflected from the setups acceptance after passing the lead block. To get an estimate of the deflection the standard deviation of the scattering angle of the muons is calculated for low momentum and high momentum muons, respectively using the following equation: There p denotes the muon momentum, c the speed of light, β the velocity over c of the muon, z the muons charge, x the thickness of the material and X_0 the radiation length of the material.

$$\theta_{ms} = \frac{13.6\text{MeV}/c}{p\beta} z \sqrt{\frac{x}{X_0}} \tag{6.7}$$

This leads for example to $\theta_{ms}(p = 320 \text{ MeV}) = 14\ °$ and $\theta_{ms}(p = 5 \text{ GeV}) = 0.9\ °$. In addition, the opening angle of the setup is calculated to $\theta_{op} = 7°$ (assuming the muon passing the detector in the centre). With that one can conclude that most muons below 320 MeV are either shielded by the lead block or deflected from the setups acceptance due to multiple scattering, because the scattering angle is way larger than the opening angle of the setup. As θ_{ms} scales with one over momentum the scattering angle decreases with higher momentum and therefore a smaller fraction of high momentum muons gets deflected from the acceptance. Meaning at some momentum nearly all muons are still measured after the lead block.

The same analysis as before is carried out with this data and the results can be seen in the following figure and table.

Configuration	Number of muons per cm^2 per 10^{12} POT
SHADOWS wall	352.2 ± 2.2 (stat.) $\pm$ 14.1 (sys.)
SHADOWS wall+lead block	280.7 ± 2.6 (stat.) $\pm$ 11.3 (sys.)

Table 6.3: Muons per cm^2 per 10^{12} POT for different configurations

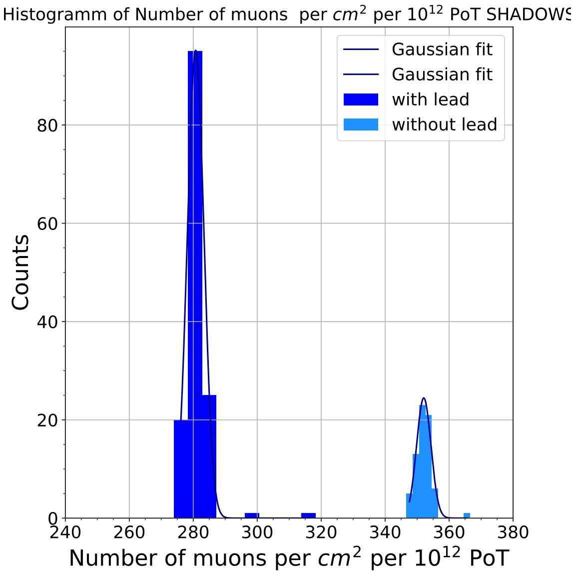

Figure 6.17: Number of muons per cm^2 per 10^{12} POT in SHADOWS-Mode with and without lead

Having a look at Table 6.3 it can be concluded that the muon flux is reduced by 20 % due to the lead block. Due to the influence of shielding and multiple scattering it can be concluded that this 20 % include most muons below 320 MeV. In addition, other low energetic muons are also included in this 20 %, because they are deflected from the setups acceptance due to multiple scattering. As the scattering angle decreases with higher momentum and gets smaller compared to the opening angle of the setup, high energetic muons are still reaching the setup after the lead block. Therefore, around 20 % of the muons are low energetic.

7. Conclusion

In this thesis the background muon flux in the ECN3 Experimental Hall at the future SHADOWS detector position is measured to validate simulations of the disturbing background. Furthermore, the result is provided for further studies.

To fulfil this goal a measurement setup using four scintillators including a WLS fibre readout on both sides by one SiPM each is developed and tested within this thesis. It is constructed and the general settings and its functionality are verified. This includes a study of the threshold settings, a measurement of the time resolution of the measurement setup, an afterpulse study and a coincidence test. The measurement setup works as expected. However, it is found that the same fibre read out on both sides in the scintillator leads to a high coincidence rate of two SiPMs. The reason for that are UV photons which are produced in the avalanche inside one SiPM and are then coupled through the WLS to the other SiPM. The problem can be overcome for the muon flux measurement by characterising a muon by demanding a hit in at least one SiPM per scintillator at the same time which suppresses the high coincidence rate in one scintillator.

Furthermore, the taken data at the future SHADOWS position is analysed to determine the background muon flux. This is done, by determining the number of muons per cm^2 per POT for every spill and normalising that to 10^{12} POT. That gives the possibility to histogram the determined numbers, fit a Gaussian and determine mean and standard deviation. The number of muons per cm^2 per 10^{12} POT in SHADOWS-Muon-Mode at the position of the muon measurement setup is determined to $352.2 \pm 2.2\,(\mathrm{stat.}) \pm 14.1\,(\mathrm{sys.})$. The results are compared with the pixel data, the data from another setup and the simulation. They agree with each other despite the expected discrepancy with the simulated data. Using a lead block to shield low energetic muons the composition of the muon flux is studied. It is shown that around 20 % of the muons reaching the setup are low energetic.

An improvement for further measurements could be achieved by changing the design of the scintillators to remove the problem with the too high coincidence rate in one scintillator. As studied in this thesis, using one readout per fibre instead of two readouts per fibre is a possible solution and reduces the coincidence rate in one scintillator.

Appendices

A. Calculated Geometrical Acceptance Loss of the Scintillator Setup

To show that the measured acceptance drop for the first and last scintillator is reasonable a calculation is carried out using the angular distribution of the muons measured with the silicon pixel telescope [11]. The probability $P(4|1 \wedge 2 \wedge 3)$ that scintillator four is hit, is calculated under the condition that scintillator one, two and three are hit keeping in mind the angular distribution of the muons.

First of all it is assumed that scintillator one is always hit. To calculate the acceptance drop of the fourth scintillator and to be able to compare the result to the measured efficiencies, the probability that scintillator four is hit is calculated under the condition that scintillator one, two and three are hit $P(4|1 \wedge 2 \wedge 3)$. To do so Bayes theorem is used [24]:

$$P(4|1 \wedge 2 \wedge 3) = \frac{P(1 \wedge 2 \wedge 3|4) \cdot P(4)}{P(1 \wedge 2 \wedge 3)} = \frac{P(4)}{P(3)} \tag{A.1}$$

The probability of $P(1 \wedge 2 \wedge 3|4)$ is equal to one, because scintillator two and three are always hit, if one and four are hit. In addition, to this the probability of $P(2 \wedge 3) = P(3)$, because scintillator 2 is always hit if one and three are.

The probability $P(4)$ and $P(3)$ are calculated from a geometrical derivation under the assumption that scintillator one is always hit. To do so it is assumed that the probability density for hitting scintillator one is constant over the area of scintillator one. Furthermore, the angular distribution $p(\theta)$ in x- and y- direction is given by a Gaussian distribution, respectively:

$$p(\theta) = \frac{1}{\sqrt{2\pi\sigma^2}} e^{-\frac{(\theta-\mu)^2}{2\sigma^2}} \tag{A.2}$$

where θ corresponds to the angle and σ and μ to the measured standard deviation and mean of the Gaussian distribution in x- and y-direction, respectively.

This calculation is done in x- and y-direction and leads to the following:

$$
\begin{aligned}
P(i) &= \int_{-\frac{l}{2}}^{\frac{l}{2}} \frac{1}{l} dx \int_{\theta_2(x)}^{\theta_1(x)} p_x(\theta_x) d\theta_x \int_{-\frac{l}{2}}^{\frac{l}{2}} \frac{1}{l} dy \int_{\theta_2(y)}^{\theta_1(y)} p_y(\theta_y) d\theta_y \\
&= \int_{-\frac{l}{2}}^{\frac{l}{2}} \frac{1}{l} dx \int_{\theta_2(x)}^{\theta_1(x)} \frac{1}{\sqrt{2\pi\sigma_x^2}} e^{-\frac{(\theta_x-\mu_x)^2}{2\sigma_x^2}} d\theta_x \int_{-\frac{l}{2}}^{\frac{l}{2}} \frac{1}{l} dy \int_{\theta_2(y)}^{\theta_1(y)} \frac{1}{\sqrt{2\pi\sigma_y^2}} e^{-\frac{(\theta_y-\mu_y)^2}{2\sigma_y^2}} d\theta_y
\end{aligned}
\tag{A.3}
$$

Where l corresponds to the length of the scintillator in x- and y- direction and θ_1 and θ_2 correspond to the minimum and maximum angle of the muons to still hit the ith scintillator. They are derived geometrically from Figure A.1.

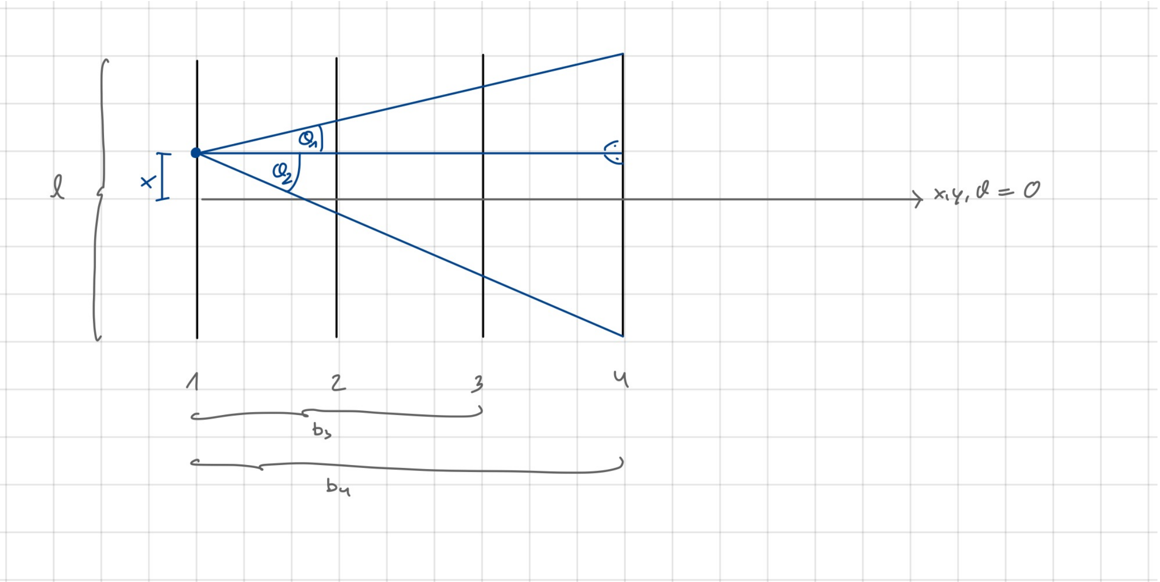

Figure A.1: Geometrical Derivation of the acceptance loss probability for $P(4)$

$$
\begin{aligned}
\tan(\theta_1) &= \frac{\frac{l}{2} - x}{b_i} \\
-\tan(\theta_2) &= \frac{\frac{l}{2} + x}{b_i}
\end{aligned}
\tag{A.4}
$$

In this case l is again the scintillator length, x the distance of the muon from zero and b_i the distance between scintillator one and i taken from Figure 5.3.

The integration in $d\theta_x$ and $d\theta_y$ is performed analytically and leads to:

$$\begin{aligned} P(i) = &\int_{-\frac{l}{2}}^{\frac{l}{2}} dx \; \frac{1}{2l} \left(\mathrm{erf}\left(\frac{\theta_1(x) - \mu_x}{\sqrt{2\sigma_x^2}} \right) - \mathrm{erf}\left(\frac{\theta_2(x) - \mu_x}{\sqrt{2\sigma_x^2}} \right) \right) \\ &\cdot \int_{-\frac{l}{2}}^{\frac{l}{2}} dy \; \frac{1}{2l} \left(\mathrm{erf}\left(\frac{\theta_1(y) - \mu_y}{\sqrt{2\sigma_y^2}} \right) - \mathrm{erf}\left(\frac{\theta_2(y) - \mu_y}{\sqrt{2\sigma_y^2}} \right) \right) \end{aligned} \tag{A.5}$$

Plugging all the numbers in and solving the other two integrals numerically gives a value for P(4) and P(3) which leads to $P(4|1 \wedge 2 \wedge 3) = 0.94$ for the portion of muons reaching the last scintillator after hitting the other three as well. Considering the efficiencies from Table 6.1 and assuming an inefficiency of the outer scintillators of 3 % as well, leaves us with $0.97 \cdot 0.94 = 0.91$ which matches the 0.92 measured for the outer scintillators in subsection 6.4. Therefore, the measured acceptance loss of the outer scintillators is reasonable.

References

[1] M. Thomson. *Modern Particle Physics*. Cambridge University Press, 2013.

[2] G. Lanfranchi, M. Pospelov, and P. Schuster. “The Search for Feebly Interacting Particles”. In: *Annual Review of Nuclear and Particle Science* 71.1 (2021), pp. 279–313. DOI: `10.1146/annurev-nucl-102419-055056`. URL: `https://doi.org/10.1146/annurev-nucl-102419-055056`.

[3] M. Alviggi et al. *SHADOWS Proposal*. 2023.

[4] Wikimedia Commons. *Standard Model of Elementary Particles*. 2023. URL: `https://commons.wikimedia.org/wiki/File:Standard_Model_of_Elementary_Particles-de.svg`.

[5] H. Kolanoski and N. Wermes. *Particle Detectors Fundamentals and Applications*. Oxford University Press, 2020.

[6] C. Gruppen. *Astroparticle Physics*. Springer Verlag, 2020.

[7] J Beacham et al. “Physics beyond colliders at CERN: beyond the Standard Model working group report”. In: *Journal of Physics G: Nuclear and Particle Physics* 47.1 (2019), p. 010501. DOI: `10.1088/1361-6471/ab4cd2`. URL: `https://dx.doi.org/10.1088/1361-6471/ab4cd2`.

[8] W. Baldini et al. *SHADOWS Expression of Interest*. 2021. URL: `https://cds.cern.ch/record/2799412`.

[9] E. Izaguirre, T. Lin, and B. Shuve. “Searching for Axionlike Particles in Flavor-Changing Neutral Current Processes”. In: *Phys. Rev. Lett.* 118 (11 Mar. 2017), p. 111802. DOI: `10.1103/PhysRevLett.118.111802`. URL: `https://link.aps.org/doi/10.1103/PhysRevLett.118.111802`.

[10] G. Lanfrachi. *Status and Plans of the SHADOWS project*. Talk. Sept. 2023. URL: `https://indico.cern.ch/event/1303571/contributions/5482376/attachments/2708706/4703125/SHADOWS_SPSC_Sept2023.pdf`.

[11] S. Bachmann et al. *Muon Flux Measurement for the Shadows Experiment*. Talk. July 2023. URL: `https://indico.cern.ch/event/1302351/contributions/5485870/attachments/2680335/4649423/MuonFluxResults.pdf`.

[12] *BC-400/BC-404/BC-408/BC-412/BC-416 Premium Plastic Scintillators*. URL: `https://www.phys.ufl.edu/courses/phy4803L/group_I/muon/bicron_bc400-416.pdf`.

[13] *Product Information, Wavelength Shifting Fibres*. URL: `https://www.kuraray.com/products/psf`.

[14] *DuPont™ Tyvek® Reflex Technical Datasheet*. URL: `https://www.dupont.co.uk/content/dam/dupont/amer/us/en/performance-building-solutions/public/documents/en/UK-IE-en-TDS-3583M.pdf`.

[15] *MPPC (Multi-Pixel Photon Counter) S13360 series*. URL: https://www.hamamatsu.com/content/dam/hamamatsu-photonics/sites/documents/99_SALES_LIBRARY/ssd/s13360_series_kapd1052e.pdf.

[16] LHCb Collaboration. *LHCb Tracker Upgrade Technical Design Report*. Tech. rep. 2014. URL: https://cds.cern.ch/record/1647400.

[17] X. Han. *Trigger Board User Manual*.

[18] A. Vacheret et al. "Characterization and simulation of the response of Multi-Pixel Photon Counters to low light levels". In: *Nuclear Instruments and Methods in Physics Research Section A: Accelerators, Spectrometers, Detectors and Associated Equipment* 656.1 (2011), pp. 69–83. DOI: 10.1016/j.nima.2011.07.022. URL: https://doi.org/10.1016%2Fj.nima.2011.07.022.

[19] S. Piatek. *Measuring the electrical and optical properties of silicon photomultipliers*. 2014. URL: https://hub.hamamatsu.com/us/en/technical-notes/mppc-sipms/measuring-the-electrical-and-optical-properties-of-silicon-photomultipliers.html.

[20] F. Ambrosino and other. *Technical Design Report NA62*. URL: https://na62.web.cern.ch/Documents/TD_Full_doc_v10.pdf.

[21] M. van Dijk and J. Bernhard. *Discussion of the Error of the POT Measurement at the K12 Beam Line*. Private Communication. 2023.

[22] F. Stummer. *Discussion of the Simulation of the Background Muon Flux at ECN3*. Private Communication. 2023.

[23] Darjani et al. In: *Indian Journal of Pure & Applied Physics Vol. 52 January* (2014).

[24] U. Schwarz. *Theoretical Statistical Physics*. Lecture Script. Feb. 2023. URL: https://www.thphys.uni-heidelberg.de/~biophys/PDF/Skripte/StatPhys.pdf.

Acknowledgements

First of all I want to thank Prof. Ulrich Uwer for giving me the opportunity to write my bachelor thesis in his working group. It was a pleasure to do so and I felt very welcomed. I also want to thank Dr. Sebastian Bachmann who worked with me throughout this thesis. Thank you for the guidance and for always answering all of my questions. I am also thankful for Lucas Dittmann who helped me a lot with my coding and in the lab. I want to thank Prof. Schultz-Coulon for being my co-supervisor. I am thankful for my boyfriend, my friends and my family for always supporting me and for proof reading my thesis.

Erklärung

Ich versichere, dass ich diese Arbeit selbstständig verfasst und keine anderen als die angegebenen Quellen und Hilfsmittel benutzt habe.

Heidelberg, den 27.11.23 ....,

C. Welschaft